Publication title	From molecular to sub-µm scale: The interplay of precursor concentrations, primary particle size, and carbon nanostructure during soot formation in counter-flow diffusion flames
Authors	Hagen, Fabian P., Vlavakis, Petros, Bockhorn, Henning, Suntz, Rainer, Trimis, Dimosthenis
Issue Date	2023
Publisher	Elsevier
Type of publication	Journal article
Acknowledgement	The ESTiMatE project has received funding from the Clean Sky 2 Joint Undertaking under the European Union's Horizon 2020 research and innovation programme under grant agreement No 821418.
Disclaimer	The content of this article reflects only the authors' view. The Clean Sky 2 Joint Undertaking is not responsible for any use that may be made of the information it contains.

Combustion and Flame xxx (xxxx) xxx

Contents lists available at ScienceDirect

Combustion and Flame

journal homepage: www.elsevier.com/locate/combustflame

From molecular to sub-μm scale: The interplay of precursor concentrations, primary particle size, and carbon nanostructure during soot formation in counter-flow diffusion flames

Fabian P. Hagen[a,b], Petros Vlavakis[a], Henning Bockhorn[a,*], Rainer Suntz[b], Dimosthenis Trimis[a]

[a] Engler-Bunte-Institute, Division of Combustion Technology, Karlsruhe Institute of Technology, Karlsruhe, Germany
[b] Institute for Chemical Technology and Polymer Chemistry, Karlsruhe Institute of Technology, Karlsruhe, Germany

ARTICLE INFO

Article history:
Received 29 April 2022
Revised 2 February 2023
Accepted 8 March 2023
Available online xxx

Keywords:
Soot formation
Counter-flow diffusion flames
Precursor concentration
Soot primary particle sizes
Carbon nanostructure
Optical properties

ABSTRACT

The focus of this work is on counter-flow diffusion flames of C_2H_4/air near the sooting limit (f_V < 500 ppb) to shed light on the transition of precursor molecules to primary soot particles and their nanostructure. The applied experimental techniques cover non-intrusive methods based on laser-induced incandescence (LII) for determination of soot volume fractions, primary particle sizes, and ratios of refractive indices for absorption at different wavelengths. The methods are complemented by intrusive methods such as sampling with microprobes and analysis of gas composition by gas chromatography and mass spectrometry, particle sizing by differential mobility analysis, and determining carbon nanostructures of particles by high-resolution transmission electron microscopy (HRTEM). For numerical simulation, the well-known ABF-model is applied.

The experimentally determined structures of the counter-flow flames could be well reproduced within the experimental uncertainties by the ABF-model for varying fuel mass fractions and strain rates. The numerical simulations identify the different processes during particle formation and the main variation can be attributed to variation of surface growth rates when applying strain rates and fuel mass fractions leading to higher soot volume fractions. Particle size distributions detected in the fuel flow near and below the stagnation plane appear bimodal with distinct maxima at particles sizes about 5 nm and 20 nm. The nanostructure of the primary particles exhibits basic structural units (BSUs), that increase up to the size of 7 Å to 10 Å at increasing soot volume fractions from about 100 ppb to 300 ppb. This coincides with the increase of the mole fractions of the detectable soot precursors with increasing soot volume fraction. The ratios of refractive index functions for absorption $E(m,\lambda_{532})/E(m,\lambda_{1064})$ and $E(m,\lambda_{266})/E(m,\lambda_{1064})$ decrease approximately linearly with increasing soot volume fractions. This is corroborated by the analyses of HRTEM-images that clearly bring about increasing sized BSUs with increasing soot volume fractions causing a shift of the absorption to larger wavelengths.

1. Introduction

The formation of soot during combustion of carbon containing fuels represents an extremely complex process. The reasons for this complexity are manifold: The formation of soot converts molecules with only few carbon atoms to soot particles containing several million carbon atoms. The underlying chemical and physical processes take place on molecular to sub-μm and μm scales. The time scales of soot formation are in the order of 5 ms < τ_{soot} < 10 ms [1], which is more than one order of magnitude larger than the characteristic time scales of combustion. Therefore, characteristic time scales of soot formation and combustion, respectively, couple differently with the hydrodynamic time scales. This interaction affects the properties of soot being formed in flames but also the use of flames to produce functional carbon-based nanomaterials.

The combustion of carbon containing fuels under sooting conditions encompasses numerous chemical reactions between a large number of chemical species, their growth to larger molecules, the dynamics of large pre-particle molecular clusters as well as phase

* Corresponding author at: Karlsruhe Institute of Technology (KIT), Engler-Bunte-Institute, Division of Combustion Technology, Engler-Bunte-Ring 7, Karlsruhe, Germany.
E-mail address: henning.bockhorn@kit.edu (H. Bockhorn).

https://doi.org/10.1016/j.combustflame.2023.112729

transitions, formation of liquid-like particles and aggregation to fractal aggregates of carbonaceous primary particles. For studying these processes, usually canonical model configurations are employed. One model configuration offering the possibility of varying the essential variables affecting soot formation (and oxidation) independently of one another consists in laminar counter-flow diffusion flames. In counter-flow diffusion flames the hydrodynamic time scales can be varied in a simple way by systematically varying the strain rate without modifying the thermochemistry of the system. Another characteristic of counter-flow flames is the possibility to stabilize the flame at different positions relative to the stagnation plane depending on the flow rates and composition of the two feed flows. Furthermore, for the numerical simulation of counter-flow flames one dimensional formulations of the balance equations are applicable [2] reducing considerably the computational expense when treating systems with large numbers of chemical species involved in a complex network of chemical reactions. For these reasons, laminar counter-flow flames have been used frequently as an important highly controllable model flame configuration for investigating soot formation and oxidation, see e.g., [3–14]. In this work, the focus is on counter-flow diffusion flames of C_2H_4/air near the sooting limit (f_V < 500 ppb) to shed light on the transition of precursor molecules to primary soot particles and their nanostructure.

Several investigations on the formation of soot in counter-flow diffusion flames of different fuels brought about that an increase of the fuel mass fraction in the fuel flow increases soot formation, whereas an increasing strain rate decreases soot formation and polycyclic aromatic hydrocarbon (PAH) formation due to reduced residence times [7–14]. Most of these studies were focused on counter-flow diffusion flames characterized by the flame located on the oxidizer side of the stagnation plane, so called soot formation flames (SF). In this configuration, the formed soot particles are convected in the direction opposite to the oxidizer stream, where soot oxidation is suppressed. The SF flames are realized at moderate oxygen mole fractions at the oxidizer side and soot formation occurs in a zone poorer in oxygen and the overall process is dominated by particle inception and particle dynamics [12–14], offering the option of focussing on the transition of precursor molecules to primary soot particles. In contrary, in configurations where the flame is located on the fuel side of the stagnation plane, soot particles are being convected in the direction of the high-temperature region towards the oxidizer stream, where soot oxidation occurs at a reasonable level [6,15], so called soot formation-oxidation flames (SFO). The SFO flame is realized in the presence of high oxygen mole fractions at the oxidizer side confining the soot formation region in a small oxygen rich zone with high temperatures. In this configuration the competition between soot inception and oxidation processes dominates soot formation.

As the focus of this study is on the interplay of precursor concentrations, primary particle size, and carbon nanostructure of primary particles during soot formation, the SF flame has been chosen as configuration for the counter-flow diffusion flames. As fuel C_2H_4 is selected because experimental data for comparison is also available from literature [14] and similar flames are the subject of discussions in the ISF-workshops [4,5,16]. This work encompasses experiments for quantifying mole fractions of gas phase species in the flames by sampling followed by analysis through Gas Chromatography and Mass Spectrometry (GC/MS). Particle characterization is performed through sampling and analysis with the help of a Scanning Mobility Particle Sizer (SMPS), which also enables the determination of soot volume fractions. Primary particle sizes and soot volume fractions are measured as well non-intrusively by Two-Color Time-Resolved Laser-Induced Incandescence (2C-TiRe-LII) allowing comparison with and validation of the SMPS results. The laser spectroscopic experiments are complemented by Three-Wavelength-Excitation Time-Resolved LII (3WE-TiRe-LII) to determine ratio pairs of refractive index functions for absorption at different wavelengths. The technique represents an extension of the approach from Therssen et al. [17]. In this work a Nd:YAG laser operating at the fundamental wavelength 1064 nm and the second and fourth harmonics (532 nm and 266 nm) has been used. From the measurements the ratios $E(m,\lambda_{UV})/E(m,\lambda_{NIR})$, $E(m,\lambda_{UV})/E(m,\lambda_{VIS})$, and $E(m,\lambda_{VIS})/E(m,\lambda_{NIR})$ are derived. The optical properties can be related to the nanostructure of the primary particles as described in [18,19]. The primary particle nanostructure is characterized by sampling soot particles from the flames and inspecting them by High-Resolution Transmission-Electron-Microscopy (HRTEM). Finally, the flames have been numerically simulated using the ABF-model for soot formation and oxidation implemented in the CHEMKIN-based code SOPHOKLES [20].

In the following section of this paper, the experimental concepts and some theoretical backgrounds of the experimental techniques are introduced. Section 3 gives a brief description of the basics of the numerical simulations. In Section 4 the experimental and numerical results are presented with focus on the interplay of precursor concentrations, primary particle size, and carbon nanostructure of primary particles. Starting from the molecular scale with the analysis of the gas phase, the characterization of the particle phase on the μm-scale and the carbon nanostructure of the primary particles on the sub-μm scale follows. Finally the results for $E(m,\lambda_1)/E(m,\lambda_2)$ are discussed and related to the carbon nanostructure of the soot particles. The paper closes with some conclusions.

2. Experiments

2.1. Counter-flow burner

The experiments have been run in the counter-flow burner configuration sketched in Fig. 1. More details are given in ref. [21]. The burner consists of two identical, opposedly placed ducts with an inner diameter of 25 mm, and a fixed separation distance L of 12.5 mm. The fuel mixture consisting of C_2H_4 and N_2 (flow rate $\dot{V}_1$) is fed through the bottom duct and the oxidizer mixture (air, flow rate $\dot{V}_2$) from the top. Both ducts are surrounded by concentric annular ducts providing a shield flow of N_2. Fine wire meshes with 50 μm wire diameter placed at the duct exits ensure approximate plug-flow inflow conditions. Oxidizer, fuel, and purge gasses of highest purity are supplied through mass flow controllers (MFCs). The exhaust gasses are removed via a separate second concentric annular duct around the fuel duct. The removal of the exhaust gasses causes slightly bending of the outer edge of the flame towards the fuel duct.

In the experiments, a momentum balance ($\rho_1 \cdot v_1^2 = \rho_2 \cdot v_2^2$) is imposed to keep the stagnation plane fixed approximately at the center between the two ducts. Due to the momentum equilibrium, the strain rate is directly correlated with the flow rate of the oxidizer mixture $\dot{V}_2$ and distance L and can be approximated by $a_2 = 4 \cdot |v_2| \cdot L^{-1}$ [21].

2.2. Investigated counter-flow diffusion flames

The investigated counter-flow diffusion flames have been adapted to the recommendations and target flames of the 5th international sooting flame (ISF-5) workshop. Ethylene served as fuel and the selected fuel mass fractions $Y_{Fuel,1}$ as well as the strain rates a_2 are similar to [4,5]. The operating conditions of the flames reported in this work are given in Table 1 and have been set close to the sooting limits. Pressure was ambient pressure and feed gas temperature was 27 °C.

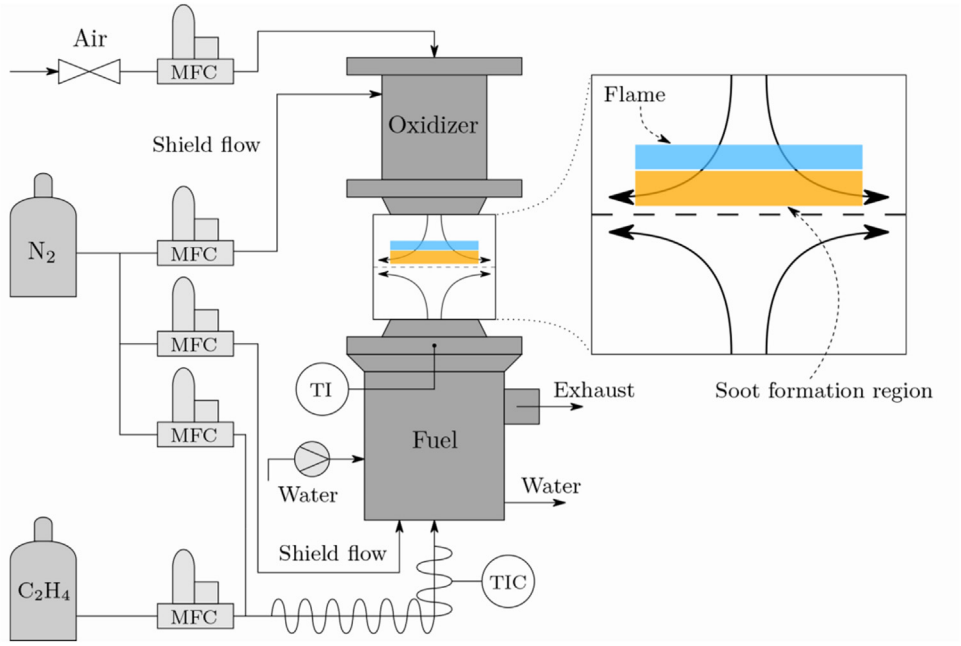

Fig. 1. Counter-flow burner used in the experiments.

Table 1
Operating conditions of the investigated counter-flow diffusion flames.

Fuel flow		Oxidizer Flow		Strain rate a_2/s^{-1}	Z_{st}
$Y_{Fuel,1}$	$Y_{N_2,1}$	$Y_{O_2,2}$	$Y_{N_2,2}$		
0.200	0.800	0.233	0.767	30, 40, 50, 60	0.254
0.250	0.750	0.233	0.767	30, 40, 50, 60	0.214
0.300	0.700	0.233	0.767	30, 40, 50, 60	0.185
0.350	0.650	0.233	0.767	60	0.163

The stochiometric mixture fraction $Z_{st} = Y_{O_2,2}/(s \cdot Y_{Fuel,1} + Y_{O_2,2}) < 0.5$ with $s = Y_{O_2,st}/Y_{Fuel,st}$ has been set to smaller than 0.5. Thereby, the diffusion flames are stabilized in the oxidizer flow relative to the stagnation plane forming a soot formation (SF) flame. As far as possible, the experimental methods described in the subsections below have been applied to the entire set of the flames. Limitations are due to the intended low soot volume fractions ($f_V < 500$ ppb), which exclude on the one hand the application of 2C-TiRe-LII and the detection of higher hydrocarbons by sampling and GC/MS analysis for flames with low fuel mass fractions and high strain rates. On the other hand, sampling of soot particles followed by analysis of particle properties by SMPS is limited by clogging of the probe for flames with high fuel mass fractions and low strain rates.

2.3. Temperature measurements

The axial temperature profiles of the investigated flames were determined with the help of thermocouples. Based on refs [22,23], a thermocouple probe with a S-type thermocouple has been developed. A fine wire (0.1 mm diameter) with a built-in spring mechanism was used fixing the thermocouple wires in parallel to the burner surface across the flame under tension to prevent deformation in the flame environment. To eliminate catalytic effects, the wires were coated with zirconia oxide. The coated thermocouple bead had a diameter of 0.4 mm. This design allows only the wires entering the flame avoiding disturbances of the reaction zone by the thermocouple. The measured temperatures were corrected for radiation losses according to [24] and assuming a spherically shaped bead with diameter d_{bead}.

$$T_{corrected} = T_g + \sigma \cdot \varepsilon \cdot T_g^4 \cdot \left(\frac{d_{bead}}{\lambda \cdot Nu} \right) \quad (1)$$

The emissivity is taken as $\varepsilon = 0.4$, the Boltzmann constant $\sigma = 5.67 \times 10^{-8}$ $W \cdot m^{-2} \cdot K^{-4}$. T_g means the gas temperature. The Nusselt number Nu due to the prevailing low convective velocities is assumed to be constant at 2.0. The thermal conductivity λ of the wire has a temperature dependency given by $\lambda = 4.6942 \cdot 10^{-3} + 8.122 \cdot 10^{-5} \cdot T_g - 1.4547 \cdot 10^{-8} \cdot T_g^2$. The uncertainties in the measured temperatures are estimated to $\pm$ 40 K, based on the standard deviations in the measured values and the uncertainties introduced due to the radiation correction procedure. The thermocouple device was mounted on a traverse system to be moved between the fuel and oxidizer ducts. The accuracy of fixing the position of the thermocouple was better than the size of the thermocouple bead (0.4 mm). The measured temperatures, therefore, reflect the conditions averaged over the size of the thermocouple bead. These uncertainties in temperature and position ($\pm$ 40 K, $\pm$ 0.4 mm) are indicated as error bars in the figures in Section 4. A visible perturbation of the flame by the thermocouple could not be observed.

2.4. Gas phase concentration measurements

For measuring the composition of the gas phase, a sampling technique similar to the concept reported in ref. [21] and described in ref. [25] has been applied. A chemically inert, deactivated ceramic probe with an inner and outer diameter of 0.3 mm and 0.5 mm, respectively, and a length of 25 mm was used. This microprobe is connected to a 1/16″ stainless steel tube, which in turn is fixed through a reducer fitting to a 6 mm stainless steel tube. The probe system is joint via a particle filter and heated lining (160 °C) to a GC/MS system (Agilent 130, GC 7890B and MSD 5977B, modified by Teckso GmbH), equipped with a thermal conductivity detector for quantifying permanent gasses (CO, CO_2, O_2, H_2O and H_2) and a flame ionization detector for hydrocarbons. A detailed description of the GC/MS system is given in [25]. To obtain axial species profiles, the probe is mounted on a traverse system and moved in steps of 0.5 mm to cover the distance between

the fuel and oxidizer ducts. The overall uncertainty in the measured concentrations is ± 3% to ± 10% for the main species (N_2, O_2, H_2, CO, CO_2, C_2H_4), ± 5% to ± 30% for light and heavy hydrocarbons, including several soot precursors (i.e., acetylene (C_2H_2), benzene (A1), and Naphthalene (A2)), and ± 20% for H_2O. These values correspond to the largest uncertainty of the species mole fractions based on the standard deviation of the measurements and the errors from the calibration of the detectors. As for the thermocouple measurements the spatial resolution is in the order of the size of the microprobe (0.5 mm). In addition, an error in the measured mole fractions arises from non-isokinetic sampling. These effects are discussed extensively in refs [26,27]. The resulting errors have been estimated in ref. [26] via CFD-simulations of the flow field around the tip of molecular beam probes. It was worked out in [26], that (i.) the sampling probe can reach a higher temperature than the gas at the sampling point, (ii.) the probe sucks in gasses from regions upstream and downstream of the probe orifice, and (iii.) the sampling leads to deformed isolines of temperature and varying streamlines. From these effects the suction of flame gasses is the governing type of perturbation of the flame structure. For the stable species sampled from flat premixed $CH_4/O_2/Ar$ flames at reduced pressure, the deviation of the simulated mole fraction profiles is in the order of magnitude of the uncertainty of mole fractions determined by mass spectrometry. Based on this, the above given maximum uncertainties in species concentrations (10% to 30%) and spatial resolution (± 0.5 mm) are indicated as error bars in the figures in Section 4. A visible perturbation of the flame, e.g. anchoring of the flame at the probe, could not be observed or operating conditions where this occurred have been avoided.

2.5. Soot sampling and characterization

For characterizing soot in the counter-flow diffusion flames probe sampling connected with SMPS and HRTEM as well as 2C-TiRe-LII and 3WE-TiRe-LII have been applied.

2.5.1. Probe sampling and SMPS

When probing soot particles from flames for tracking the evolution of particle properties, a rapid dilution of the particle-laden gas sampled from the flame is of paramount importance to quench all processes affecting particle size distributions, coagulation and diffusion of particles or surface reactions [3,28-30]. Consequently, the sampled flame gasses need to be mixed immediately after entering the probe with a high quantity of inert diluent. Sampling methods applied to premixed laminar flames are reported in refs [28–30] and for turbulent premixed flames in ref. [31]. The particle sampling system used in this work is similar to that in ref. [31] and consists of a dilution gas supply, a tailored quartz probe, and an exhaust gas flow and pressure control system of the diluted particle-laden gas sample. A sketch of the sampling probe is given in Fig. 2. More details are provided in [32].

The dilution gas supply comprises two MFCs. Pure N_2 is used as inert dilution gas. The primary dilution with a volume flow of $\dot{V}_{D,1}$ enters the quartz probe directly between the tip of the outer tube and the inner tube. The secondary dilution with $\dot{V}_{D,2}$ further dilutes the sampled aerosol at the exit of the quartz probe. Pressure and temperature of the sampled gasses are monitored.

The dimensions of the probe are given in Fig. 2. The concentric tubes were chosen to minimize the distance between the tips of the inner and outer tubes to less than 1.0 mm, allowing optimal and immediate quenching of the particle-laden flame gas. A pressure gage tube with an inner diameter of 0.8 mm is attached less than 1.0 mm from the tip of the outer tube. The quartz probe is installed on a motor driven traverse system enabling an exact two-dimensional positioning and sampling at different heights above

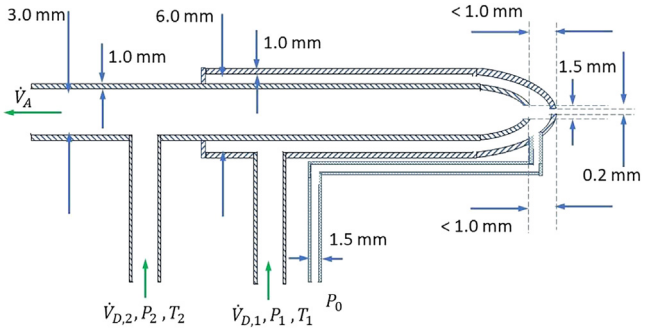

Fig. 2. Schematic drawing of the particle sampling probe.

the fuel duct (HAFD) with an accuracy of ± 0.5 mm and at different positions within the flame. For particle sampling, a primary flow rate of $\dot{V}_{D,1}$ = 4.1 l·min^{-1} is selected. At the tip orifice of the probe, a pressure drop of $\Delta P_0 = P_\infty - P_0$ of 10 Pa is set using the control valve, where P_∞ = 1 atm. Before entering the SMPS the aerosol samples are further diluted with $\dot{V}_{D,2}$ = 5.0 l·min^{-1}. The SMPS setup, see, e.g., [33,34] for theory and methodology, comprises an electrostatic classifier (EC, TSI model 3938), a soft X-ray neutralizer (TSI model 3088), a nano-differential mobility analyser (Nano DMA, TSI model 3085A), and a condensation particle counter (CPC, TSI model 3776). The EC was operated at a sheath flow rate of 15 l·min^{-1}, while the CPC was operated with $\dot{V}_A$ = 1.5 l·min^{-1}.

In addition to disturbances of the flow field and temperatures, which cool the flame and affect gaseous species concentrations and consequently soot particle properties, the particle properties change due to thermophoretic deposition and reactions within the probe [28,29]. The developed quartz probe represents a compromise between rapid quenching of the extracted sample and perturbation of the flame, elaborated by preliminary experiments with differently modified probe geometries. In the final design, the tip cone and inner tube form a minimum distance ensuring an immediate quenching. Otherwise, the detection of particles with d_m < 5 nm was not possible. Besides these systematic errors, SMPS measurements inherently include some systematic errors. Particle size distributions $P(d_m)$ measured via SMPS need to be corrected for particle losses by particle deposition in the quartz probe, the pipelines and SMPS. This is estimated using correlations proposed by Hinds [33] for laminar and turbulent flow regimes. Since mobility sizes may overestimate the size distributions due to inherent limitation of the empirical Cunningham slip correction, transformation of $P(d_m)$ into $P(d_p)$ requires some scaling as discussed in [29]. Applying the scaling for soot sampled in the flame with $Y_{Fuel,1}$ = 0.3 and a_2 = 40 s^{-1} at HAFD = 5.5 mm shifts f_V by less than 0.5% and is therefore neglected. Using the correlations proposed by Kelesidis and Pratsinis [35] accounting for fractal aggregate morphology results in an overestimation of f_V by 10% to 50%, depending on the assumed primary particle size and flame condition. Because the agreement between LII and SMPS results is reasonable, no corrections have been applied. More discussion on these aspects is given in [32]. The estimation of the CMDs from the measured $P(d_m)$ has been performed using log-normal shapes of the distributions with variable standard deviations without transformation of $P(d_m)$ to $P(d_P)$. The bimodal shape of the size distributions detected below the stagnation plane in the fuel flow produces some bias when calculating the CMDs using a log-normal approximation.

An essential parameter for correlating the absolute mobility particle size distributions and particle number densities in the flame is the dilution ratio (DR). In this work, the approach proposed by Camacho et al. is followed, measuring CO_2 concentra-

tions of samples taken from a gas flow of pure CO_2 and/or a CO_2-diluted and stabilized premixed flame [30]. By varying the pressure drop ΔP_0 at the tip orifice of the probe, DR can be systematically adjusted. Experiments with a C_2H_4 counter-flow diffusion flame ($Y_{Fuel,1} = 0.3$ and $a_2 = 60\ s^{-1}$) proved mobility particle size distributions and particle number densities being independent of ΔP_0 and, therefore DR, in the range from 10 Pa to 250 Pa [32]. To ensure optimal quenching of the flame gasses, $\Delta P_0 = 10$ Pa resulting in DR $\approx$ 800 has been selected for the experiments, see also discussion in ref. [32]. Summing up the uncertainties in the DR, disturbances of the flame, particle deposition in the probe and tubing, and transformation of the SMPS signals results in estimates of the accuracy of the measured soot volume fractions and mean particle sizes of $\pm$ 30%. These uncertainties in soot volume fractions and particle sizes and probe positioning ($\pm$ 0.5 mm) are indicated as error bars in the figures in Section 4. As for the experiments with thermocouples and gas phase sampling, operating conditions with visible perturbations of the flame have been avoided.

2.5.2. Soot sampling and HRTEM

For determining the nanostructure of soot particles generated in the counter-flow diffusion flames, soot particles have been deposited from inside the flame directly onto carbon coated copper TEM-grids using a fast insertion technique similar to that reported in refs [36–38]. Soot particles are driven thermophoretically to the cold TEM-grid mounted on a grid holder and are captured on the cold grid structure. The insertion system was mounted on a motor driven traverse system. The sampling time was adjusted within the range 50 ms to 250 ms to suit the soot level in the different flames. The orientation of the TEM-grids was parallel to the flow direction at the duct outlets. Therefore, the spatial resolution is in the order of the size of the TEM-grids (3.05 mm diameter) and no axial HAFD-profiles have been attained. The TEM-grids were placed at the locations of peak soot volume fractions.

HRTEM images were acquired using a Philips CM200 transmission electron microscope (ThermoFischer Scientific Inc.), operated at 200 kV and a maximum magnification of 380.000 resulting in highest spatial resolution of 0.0283 nm·px^{-1}. The carbon nanostructure of the investigated soot samples was evaluated from the HRTEM images using an image analysis algorithm for quantitative and reproducible analysis of the carbon nanostructure. The algorithm evaluates the nanostructure from different HRTEM images of the same soot sample. In this way, more than 10.000 graphene-like basic structural units (BSUs) have been analysed. The method allows quantification of the size L_f, curvature T_f, and separation distance $D_{s,f}$ of the graphene-like BSUs. Due to the large numbers of evaluated primary particles and fringes, values of the variances of the calculated properties are accessible and displayed as error bars in the respective diagrams in Section 4. A detailed explanation of the algorithm is given elsewhere [39].

2.5.3. Soot particle characterization via 2C-TiRe-LII and 3WE-TiRe-LII

In completion of the applied soot particle characterization methods, the 2C-TiRe-LII as a non-intrusive laser-based diagnostic has been applied to the investigated counter-flow flames. A schematic of the optical set-up is displayed in Fig. 3. The TiRe-LII theory applied in this work is based on the energy balance of a single spherical particle during LII [40–44]

$$\frac{d\left(\frac{\pi\ c_s\ \rho_P\ d_P^3}{6}\ T_P\right)}{dt} = \dot{Q}_{abs} - \dot{Q}_{rad} - \dot{Q}_{cond} - \dot{Q}_{evap}, \tag{2}$$

where the change of internal energy of the particle is balanced by the absorbed laser energy $\dot{Q}_{abs}$ and the energy losses caused by heat transfer ($\dot{Q}_{cond}$), radiation ($\dot{Q}_{rad}$) and evaporation ($\dot{Q}_{evap}$). In Eq. (2) c_s represents the temperature dependent specific heat and ρ_P the density of the particle. In the 2C-TiRe-LII approach, the temperature T_P is measured by the ratio of the thermal radiation intensities of the particles at two wavelengths. In this case, only the LII signal decay must be monitored and the term $\dot{Q}_{abs}$ cancels [40–44]. Applying Planck's law combined with the emissivity for soot particles and assuming Wien's approximation, i.e. $\exp(h\ c_0/k_B\ \lambda_d\ T_P) >> 1$ [43,44], the particle temperature T_P can be calculated from the ratio of the thermal radiation intensities at two different detection wavelengths λ_d^i and λ_d^{ii},

$$T_P = \frac{hc_0}{k_B}\left(\frac{1}{\lambda_d^{ii}} - \frac{1}{\lambda_d^{i}}\right)\left[\ln\left(\frac{S(\lambda_d^{i},\ T_P)}{S(\lambda_d^{ii},\ T_P)}\ \frac{E(m,\lambda_d^{ii})}{E(m,\lambda_d^{i})}\ \left(\frac{\lambda_d^{i}}{\lambda_d^{ii}}\right)^6\right)C_{cal}\right]^{-1}, \tag{3}$$

where $S(\lambda_d^{i},\ T_P)$ and $S(\lambda_d^{ii},\ T_P)$ are the radiation signals of the particles at the two different detection wavelengths after the nanosecond laser heating [41,43-45], here $\lambda_d^{i} = 450$ nm and $\lambda_d^{ii} = 650$ nm. $E(m, \lambda)$ is the refractive index function for absorption. The calibration constant C_{cal}, which accounts for the spectral sensitivity of the detection system at the two wavelengths, can be determined using a tungsten lamp. The model from refs [44,46] to compute the remaining terms on the right-hand side of Eq. (2) is used in this work.

For homogeneous and optically thin conditions inside the probe volume, the intensity of thermal radiation $S(\lambda_d,T_P)$ of the heated soot particles at a discrete detection wavelength λ_d follows Planck's radiation law integrated over all solid angles [41,42,45,47-51]:

$$S(\lambda_d,\ T_P) = \int_0^\infty \left[N_P \cdot P(d_P)\frac{8\ \pi^3 d_P^3\ h\ c_0^2\ E(m,\lambda_d)}{\lambda_d^6}\right.$$
$$\left.\left[\exp\left(\frac{h\ c_0}{\lambda_d\ k_B\ T_P}\right) - 1\right]^{-1}\ \Sigma_{\lambda_d}\right] dd_P. \tag{4}$$

The spectral response of the signal collection system is accounted via Σ_{λ_d}. Further, k_B is Boltzmann's constant, h Planck's constant and c_0 the speed of light. Finally, $P(d_P)$ represents the size distribution function of the particle ensemble within the probe volume specified as a log-normal distribution function [42,49] and N_P the total particle number. From Eq. (4) the LII signal appears to be proportional to the absolute soot volume fraction f_V. The calibration constant Σ_{λ_d} contained in Eq. (4) is obtained by calibrating the experimental setup (see below).

The temperature rise of a single particle in the Rayleigh size regime heated by absorption of a nanosecond laser pulse, see first term on the rhs. of Eq. (2), is given by

$$\dot{Q}_{abs}(\lambda_i) = \frac{\pi^2\ d_P^3\ E(m,\lambda_i)\ f_i}{\lambda_i} \tag{5}$$

if the heating of the particle is induced by a laser pulse of few nanoseconds duration and conductive, radiative, and evaporative cooling mechanisms can be excluded [52]. $\dot{Q}_{abs}(\lambda_i)$ describes the absorbed laser energy of the laser pulse with the laser fluence f_i at an irradiation laser wavelength λ_i causing heating of the particle from T_{P0} to $T_{P,max}$. If the particle is irradiated after cooling with a second laser pulse of different wavelength λ_j and accommodated laser fluence, thereby achieving coincidence of both LII peak signals, the absorbed heat fluxes and, therefore, the maximum particle temperatures resulting from the two consecutive laser pulses are equal, see Eq. (6):

$$\dot{Q}_{abs}(\lambda_i) = \dot{Q}_{abs}(\lambda_j),\ T_{P,max}(\lambda_i) = T_{P,max}(\lambda_j). \tag{6}$$

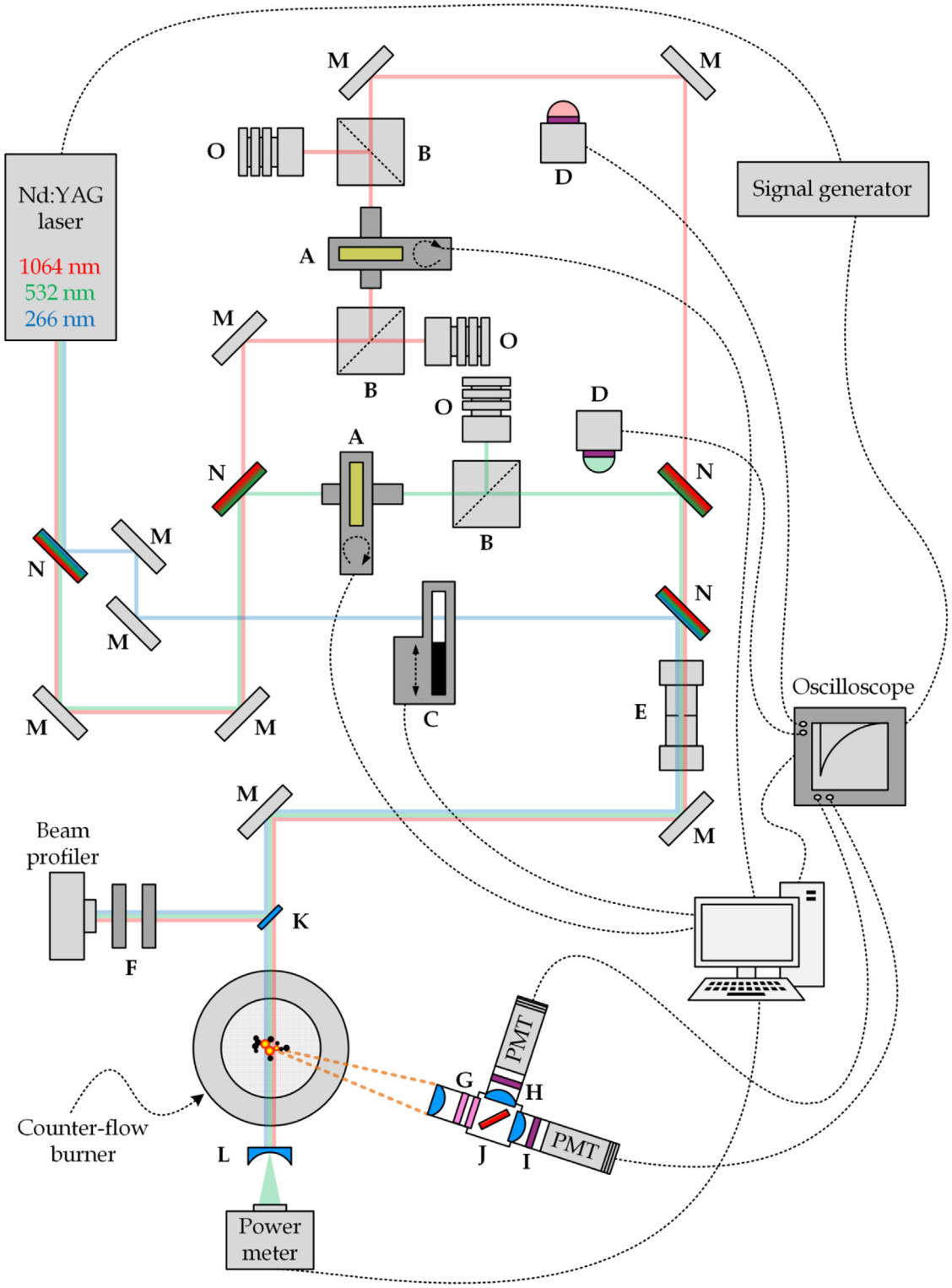

Fig. 3. Optical set-up for the Two-Color Time-Resolved Laser-Induced Incandescence (2C-TiRe-LII) and the Three-Wavelength-Excitation Time-Resolved Laser-Induced Incandescence (3WE-TiRe-LII) method. A: Rotating λ/2 Plate, B. Polarizing beam splitter, C: Beam shutter, D: Photodetector, E: Diaphragm with Ø 1 mm, F: ND-Filter, G: Notch filter, H: Bandpass filter @450 nm, I: Bandpass filter @650 nm, J: Dichroic mirror, K: Beam sampler, L: Plano concave lens, M: Mirror, N: Beam splitter, O: Beam dump.

Rearranging Eq. (5) for the condition specified by Eq. (6) results in

$$\left[\frac{E(m,\lambda_i)\ f_i}{\lambda_i}\right]_{S_{max}(T_{P,max})} = \left[\frac{E(m,\lambda_j)\ f_j}{\lambda_j}\right]_{S_{max}(T_{P,max})} . \quad (7)$$

Consequently, the ratio of the refractive index functions for absorption at the two LII excitation laser wavelengths can be determined from the required fluences of the λ_i and λ_j laser pulses according to Eq. (8) [18].

$$\frac{E(m,\lambda_i)}{E(m,\lambda_j)} = \frac{\lambda_i\ f_j}{\lambda_j\ f_i} . \quad (8)$$

From the TiRe-LII experiments threefold particle properties can be gathered: (i.) The 2C-TiRe-LII signal decay in the low laser fluence regime provides quantitative information about the size distribution of the primary soot particles $P(d_P)$, see e.g., [50,51] and references therein. The 2C-TiRe-LII signal decay is numerically computed according to Eq. (4) using the experimentally determined particle temperatures according to Eq. (3). The size distributions $P(d_P)$ are determined by a multidimensional nonlinear fit of the calculated size distributions to the measured LII signals. Approximating the size distributions by log-normal distribution functions, the first and second moments of the distribution are determined. (ii.) Soot volume fractions are obtained from the 2C-TiRe-LII- signals employing Eq. (4) and (iii.) the ratio of the refractive index functions for absorption at two LII excitation laser wavelengths according to Eq. (8) are determined employing a 3WE-TiRe-LII experiment. The experimental procedure for the 3WE-TiRe-LII experiment is briefly described below.

In the experiments a 10 Hz-pulsed Nd:YAG laser (Quanta Ray Pro 250, Spectra Physics) operating at the fundamental wavelength 1064 nm and the second and fourth harmonics (532 nm and 266 nm) has been used, see Fig. 3. The laser beam is separated into three beams of the different wavelengths at λ_{NIR} = 1064 nm, λ_{VIS} = 532 nm, and λ_{UV} = 266 nm. The beams at 1064 nm and 532 nm each pass through rotating λ/2 plates with precisely controlled rotation speeds. The subsequent polarization beam splitter reflects the s-polarized component into a beam dump while allowing the p-polarized component to pass through. Due to the continuous rotation the λ/2 plates generate periodically modulated laser fluences at λ_{NIR} = 1064 nm and λ_{VIS} = 532 nm. The single laser pulses are monitored by the Rayleigh scattered light normal to the beam path using two fast (1.0 ns and 2.3 ns rise time) photodetectors (PDA10A2 and PDA36A2, Thorlabs Inc.) equipped with bandpass filters with 10 nm FWHM centered at 532 nm and 1064 nm. This procedure allows a pulse-to-pulse evaluation of the energy density for each of the modulated laser pulses within the low-fluence regime (0.05 J·cm^{-2} < f < 0.2 J·cm^{-2} depending on the wavelength) to avoid soot evaporation. The beam at λ_{UV} = 266 nm is directed without modulation into the flame. The TiRe-LII signals were collected at 120° angle to the laser beam using a lens system and two fast photomultipliers (t_{rise} = 0.5 ns) equipped with 10 nm FWHM bandpass interference filters centered at 450 nm and 650 nm, respectively. The laser power was continuously measured with a power-meter.

The measurement routine of the 3WE-TiRe-LII is automated and applied to all experiments. To start the measurement, the beam shutter for the beam with λ_{UV} opens, and the λ/2 plates are in zero position reflecting the beams of the wavelengths λ_{NIR} and λ_{VIS} into the beam dump. The TiRe-LII induced by λ_{UV} is detected for 300 laser pulses, simultaneously recording the corresponding fluences by the power meter. After closing the beam shutter for the beam with $\lambda_{UV,}$ the λ/2 plate associated with λ_{VIS} starts rotating. The fluence modulation is reflected analogously in the detected TiRe-LII signals. For 1200 laser pulses, the TiRe-LII signals induced by λ_{VIS} are acquired. Then, the rotation of the λ/2 plate associated with λ_{NIR} starts, and 1200 TiRe-LII signals induced by varying fluences are recorded as well.

To determine the three ratios of the refractive index function for absorption $E(m,\lambda_{UV})/ E(m,\lambda_{VIS})$, $E(m,\lambda_{UV})/ E(m,\lambda_{NIR})$ and $E(m,\lambda_{VIS})/ E(m,\lambda_{NIR})$, it is mandatory to match the time-resolved decay of the signals at the corresponding wavelengths as explained in detail in refs [17,18,53]. Obtaining matches, the oscillating TiRe-LII signals induced by different fluences and wavelengths are correlated with each other. It is compulsory that the TiRe- LII signals were induced by pulses in the low-fluence regime. According to refs [17,50,53], this holds for $f(\lambda_{UV})$ < 0.1 J/cm^2, $f(\lambda_{VIS})$ < 0.15 J/cm^2, and $f(\lambda_{NIR})$ < 0.25 J/cm^2. According to these limits the maximum laser fluences $f(\lambda_{VIS})$ and $f(\lambda_{NIR})$ where adjusted by the applied polarization beam splitters. The fluence $f(\lambda_{UV})$ for the fourth harmonic of the used Nd:YAG-laser was below that limit. Fitting of the fluences to the abovementioned limits was controlled by a power meter. For coincidence better than 95% of TiRe-LII signals from two different laser excitation wavelengths λ_1 and λ_2, $E(m,\lambda_1)/E(m,\lambda_2)$ can be calculated from Eq. (8) and the fluences required to generate the matching signals. The subsequent averaging of all $E(m,\lambda_1)/ E(m,\lambda_2)$ determined from the matching signals yields the final ratio including the standard deviation for each measurement. The TiRe-LII signals induced by λ_{UV} and λ_{VIS} are analyzed comparable to Therssen et al. [17] and Yon et al. [53] after an offset time of 50 ns after absorption of the laser pulse to avoid interferences with fluorescence signals from soot precursor molecules in the UV–VIS range.

In the experiments for (i.) and (ii.) solely the signals exited at λ_{NIR}=1064 nm at constant power are used and the beam paths for the other wavelengths are shut. In the experiments for (iii.), the procedure as described above is performed. The beams of the different laser wavelengths are combined using harmonic beam splitters and optical mirrors. To ensure a coincidence of the radial irradiance profiles for the UV, VIS, and NIR laser wavelengths, the spatial distribution of the laser beam profiles is monitored using a beam profiler (WinCamD-LCM-UV) and the central part of the Gaussian laser beam is selected using a ceramic diaphragm with a diameter of 1 mm positioned inside an aluminum tube guaranteeing homogeneous fluences across the laser beam, see also [19].

The beam diameter of 1 mm causes an averaging of the results over this distance. Due to the slight bending of the flame edge towards the fuel duct a marginal tailing of the HAFD profiles in the direction of the fuel duct is expected. To convert the 2C-TiRe-LII signals into soot volume fractions, calibration by laser light extinction has been employed [32]. For this purpose, on the one hand a soot aerosol from a graphite spark discharge generator combined with a calibrated SMPS has been used. On the other hand, use of a premixed flat C_2H_2/O_2/Ar flame with equivalence ratio of 1.8 and two C_2H_4/air flames with equivalence ratio of 2.1 and 2.5, respectively was made. The calibration experiment and optical equipment for laser light extinction resembles the ones used in refs [6,14], applying a HeNe-laser at 633 nm. The soot volume fractions in the aerosol and the flame have been adjusted to the volume fraction expected in the counter-flow flames (f_V < 1000 ppb). In the calibration experiments, soot volume fractions f_V are obtained from the measured absorbance

$$f_V = \frac{-\lambda \cdot \ln\left(\frac{I}{I_0}\right)}{6 \cdot \pi \cdot E(m,\lambda) \cdot L} \,. \tag{9}$$

For the calibration the refractive index function of absorption is a critical property depending on soot particle properties and particularly soot aging. Particle properties and thereby the refractive index function varies with strain rate a_2 and $Y_{Fuel,1}$, see Section 4.3. Values ranging from about 0.152 [54] to about 0.37 [55] are reported for flame generated soot. For a given absorbance then f_V ranges within ± 40%. In this work $E(m.\lambda)$ = 0.228 [56], which is consistent with the results from 3WE-TiRe-LII, has been used for calibration. In the 2C-TiRe-LII experiments at least 600 single laser pulses have been used for evaluation providing the targeted quantities and their standard deviations. An uncertainty of ± 40% related to the uncertainty in $E(m,\lambda)$ is indicated as error bars in the respective diagrams in Section 4. This uncertainty exceeds the standard deviation of the LII signals and a possible effect of beam steering, which is estimated in [14] to ± 10%.

According to the discussion in [57] it should be noted that the accuracy and sensitivity of the different non-intrusive optical and intrusive non-optical diagnostics applied in this study depend on the nanostructural properties of soot. The optical methods, e.g., are

unsensitive to liquid like nascent soot particles and soot particles without regions of ordered, graphene-like structures neither absorb light at λ_{VIS} for laser extinction and λ_{NIR} for laser induced incandescence nor emit light at 450 nm $< \lambda <$ 650 nm. This deficiency is eliminated by using sampling methods. Primary soot particle sizes measured by 2C-TiRe-LII agree well with soot particle sizes evaluated from HRTEM-images, however, HRTEM relies also on extended regions with high nanostructural order.

3. Numerical simulations

To supplement the experimental results, the investigated flames have been numerically simulated employing the widely adopted ABF-model for combustion of C_1-/C_2-hydrocarbons and soot formation/oxidation [20]. The ABF-model – similar to models for soot formation found in the literature, see e.g. [6,14,58,59] – comprises three main modules: i) A reaction mechanism describing the oxidation of the fuel including the formation of higher hydrocarbons, ii) the treatment of the formation of particles and particle dynamics, and iii) the description of the increase/consumption of the formed soot by surface growth/oxidation reactions.

(i) Combustion of C_2H_4 is based on the extended GRI-mechanism 3.0 describing the pyrolysis and oxidation of H_2, C_1- and C_2-hydrocarbons, the formation of higher, linear hydrocarbons up to C_6, the formation of benzene (A1) and phenyl (A1-) and PAHs up to pyrene and their oxidation [60]. The mechanism encompasses three main routes to the first aromatic ring (A1) via reactions of the n-C_4H_3- and n-C_4H_5-radicals with C_2H_2 (n-C_4H_3 + C_2H_2 $\leftrightharpoons$ A1-, n-C_4H_5 + C_2H_2 $\leftrightharpoons$ A1+H) and the recombination of the propargyl radical C_3H_3 (C_3H_3 + C_3H_3 $\rightarrow$ A1). The formation of A2 occurs mainly via the addition of C_4H_4 to A1- (A1- + C_4H_4 $\leftrightharpoons$ A2 + H), while the main channel to A3 consists of ring condensation to biphenyl (P2) followed by addition of C_2H_2 (A1- + A1 $\leftrightharpoons$ P2, P2- + C_2H_2 $\leftrightharpoons$ A3 + H). The formation of pyrene (A4) proceeds one the one hand via the H-abstraction-C-addition (HACA) sequence along with ring-combination reactions. The HACA sequence is described as an infinite polymerization process with the technique of linear lumping yielding PAHs up to infinite size. On the other hand, alternative routes to A3 and A4 consist of the addition of C_4-species to A2- (A2- + C_4H_2 $\leftrightharpoons$ A3, A2- + C_4H_4 $\leftrightharpoons$ A3 + H) and the C_2H_2 and C_4H_2 addition to acenaphthylene (A2R5) (A2R5 + C_2H_2 $\rightarrow$ A3-, A2R5 + C_4H_2 $\rightarrow$ A4), ascribing an important role to A1, A2, and A2R5 as intermediate in the formation of PAHs and soot. The application of the mechanism even to complex mixtures such as producer gas has been demonstrated in [21]. The mechanism is restricted to the combustion of small aliphatic hydrocarbons and mixture compositions yielding moderate PAHs concentrations during combustion. Recent developments in reaction mechanisms specifically tailored to the combustion of higher hydrocarbons, aromatic hydrocarbons and mixtures of them, e.g. [6,14,58,61-64] provide more detailed description of the formation of higher PAHs. However, due to the use of C_2H_4 as fuel and the near sooting limit conditions of the investigated flames, the mechanism from the ABF-Model containing 101 chemical species and 545 reactions is used in the present study.

(ii) Formation of particles and particle dynamics (soot particle inception, particle coagulation, PAH adsorption) are treated by solving the Smoluchowski master equations [65] with the method of moments [66] covering all coagulation regimes (free-molecular, continuum, and transition) as well as aggregation into fractal particles [67]. Collisions of A4 and PAHs to infinite size and forming thereby larger species of larger mass are considered as particle inception. Consequently, particle inception is not restricted to the formation of isosized dimers of e.g. A4, but includes particles from differently sized PAHs. The advantage of the approach is, that particle inception, particle coagulation and PAH adsorption on soot particles can be treated via the same formalism including these processes in the source terms of the moment balance equations. The source terms then contain non-integer moments, which have to be closed by interpolation (MOMIC: method of moments with interpolative closure). The disadvantage of the method is, that only the moments of the particle size distributions are calculated. This is different to soot formation models, which approximate the particle size distributions by sections and solve particle balances for the sections, e.g. [6,58], or employ the hybrid method of moments HMOM [59]. A systematic assessment of MOMIC with guidelines for its application to soot particle dynamics in laminar and turbulent flames is provided in [68].

(iii) Surface growth and oxidation in the ABF model are described also through the HACA-sequence and oxidation by OH and O_2. The reaction sequence consists essentially of the six reactions C_{soot}-H + H $\leftrightharpoons$ C_{soot}*+ H_2, C_{soot}-H + OH $\leftrightharpoons$ C_{soot}*+H_2O, C_{soot}* + H $\rightarrow$ C_{soot}-H, C_{soot}* + C_2H_2 $\rightarrow$ C_{soot}-H + H, C_{soot}* + O_2 $\rightarrow$ 2 CO + products, C_{soot}-H + OH $\rightarrow$ CO + products, see [20]. This sequence is also implemented in soot formation models using different components in (i) and (ii), see e.g. [14] and [6] with extension by H-abstraction through CH_3, C_2H_3, and C_2H, and also [58].

The numerical simulations are based on the CHEMKIN collection of routines [69] for solving the one-dimensional balance equations for total mass, mass of chemical species, and energy extended by the balance equations for the first two moments of the soot particle size distribution. Thermophoretic transport of particles, radiation of soot and recoupling of the surface reactions to the gas phase by including the formation/consumption rates of the involved species in their mass balances has been considered. All rate coefficients and parameters were set as in ref. [20]. The parameter α describing the variation of sites accessible for surface reactions with soot particle aging has been set to 1 and the rate of oxidation of soot by O_2 has been increased slightly.

4. Results and discussion

4.1. Gas phase chemistry

As examples of the structure of the counter-flow diffusion flames, the axial profiles of temperature and species mole fractions as measured and calculated for the flames with mass fractions of fuel $Y_{Fuel,1}$ = 0.25 and $Y_{Fuel,1}$ = 0.35 at a_2 = 60 s^{-1} are displayed in Figs 4a to 4d. The error bars indicated in the figures represent estimations according to the spatial resolution and accuracy of the measurements (see Section 2.4). The flames stabilize in the oxidizer flow at about 1.5 mm upwards of the stagnation plane in the region of peak temperature. As expected, the oxidation of C_2H_4 first leads to H_2 and CO followed by the formation of CO_2 and H_2O. The fuel is successively converted partly to C_2H_6 and C_2H_2, the latter, according to the reaction mechanism of the ABF-model, contributes essentially via reactions with n-C_4H_3- and n-C_4H_5-radicals to the formation of the first aromatic ring A1. The predictions of temperature and species mole fractions agree very well with the experimental values within the margin of experimental errors. Particularly, the predicted mole fractions of C_2H_2, A1, A2R5, and A2, which are in the concept of the ABF-model most

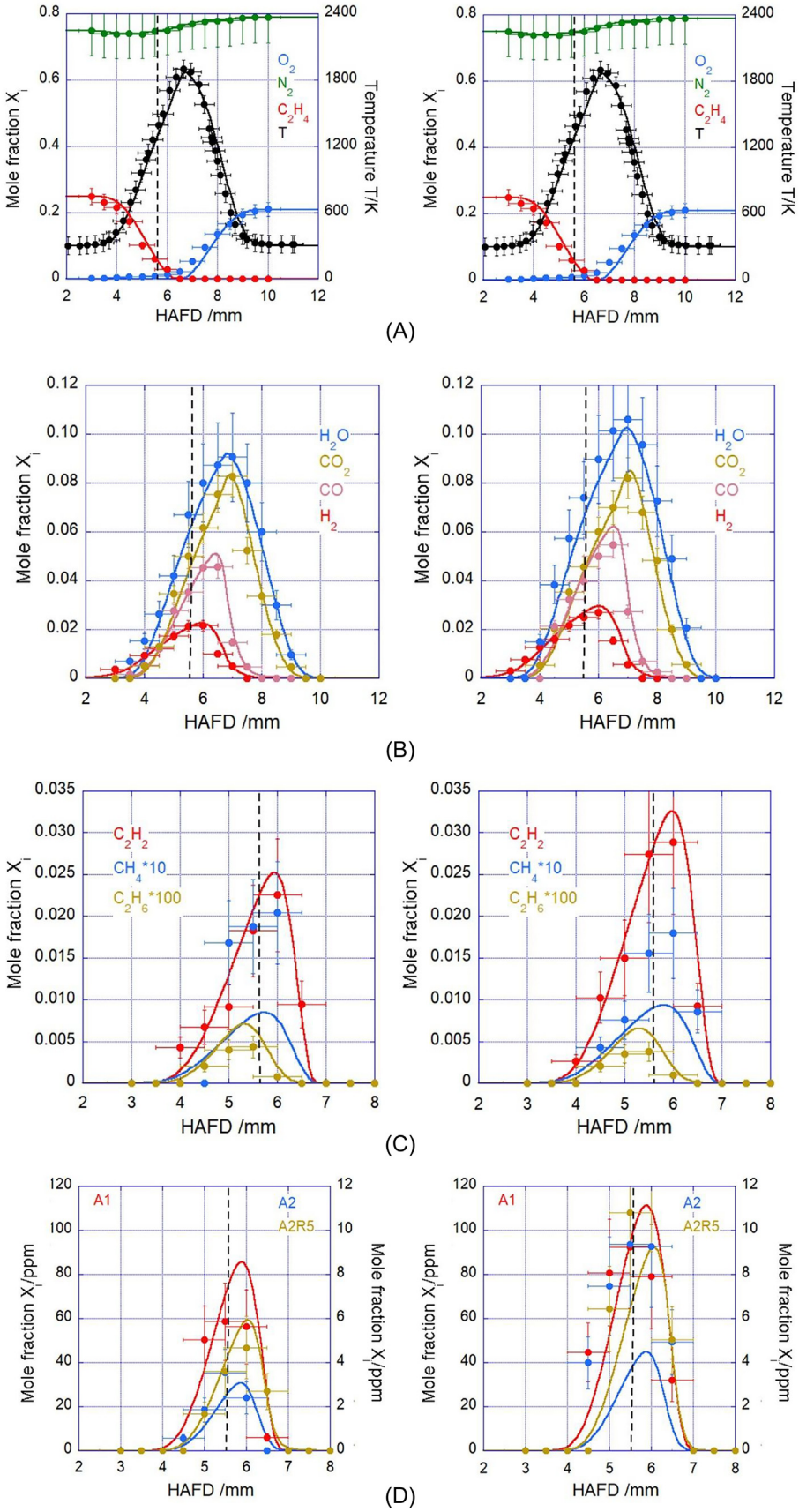

Fig. 4. (A)**:** Axial temperature and O_2, N_2, C_2H_4 mole fraction profiles for the counter-flow diffusion flames with mass fraction $Y_{Fuel,1} = 0.25$ (left), $Y_{Fuel,1} = 0.35$ (right) and $a_2 = 60\ s^{-1}$; symbols indicate experimental results, error bars represent estimations of uncertainties according to the spatial resolution and accuracy of the measurements; lines represent numerical simulations; the stagnation plane is indicated by the black dotted line. (B)**:** Same as Fig. 4(A) for H_2O, CO_2, CO and H_2. (C): Same as 4(A) for C_2H_2, CH_4, and C_2H_6. (D): Same as 4(A) for A1, A2 and A2R5.

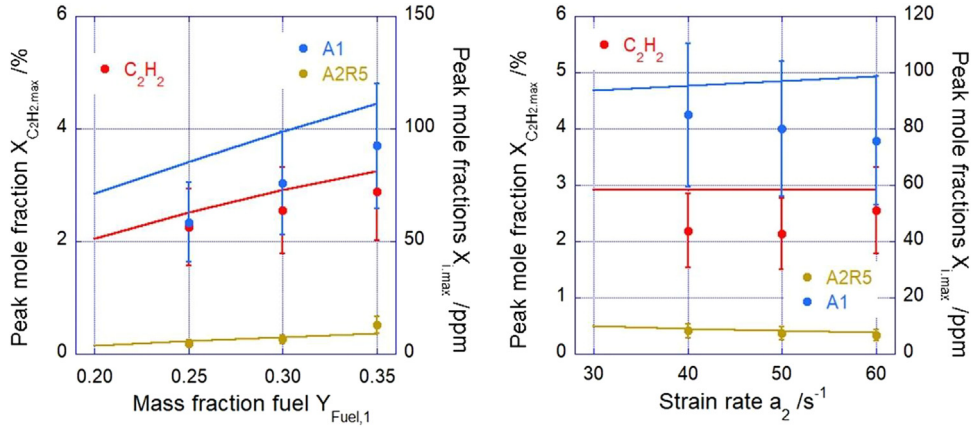

Fig. 5. Peak mole fractions of C_2H_2, A1, and A2R5 in dependence on $Y_{Fuel,1}$ at strain rate $a_2 = 60\ s^{-1}$ (left) and in dependence on a_2 at $Y_{Fuel,1} = 0.30$ (right); symbols indicate experimental results, error bars represent estimations of uncertainties according to the accuracy of the measurements; lines represent numerical simulations.

important soot precursors, agree well with the experimental ones. An exception that can be traced back to the applied reaction mechanism is CH_4, where the predictions underestimate the measured mole fractions by a factor of about 0.5.

The main conversion occurs ca. 1.5 mm to 3.5 mm above of the stagnation plane. The variation of temperature and mole fractions of the measured species in comparison with the predictions when varying $Y_{Fuel,1}$ is clearly recognizable from the figures. The slight dissymmetry of the species mole fraction profiles of the intermediate species is due to diffusional transport of the species below the stagnation plane, where the chemical reactions are weakened. This is particularly obvious from the H_2 mole fraction profiles.

The variation of the peak mole fractions of the soot precursors C_2H_2, A1 and A2R5 with $Y_{Fuel,1}$ at constant strain rate a_2 of 60 s^{-1} and with strain rate a_2 at constant $Y_{Fuel,1}$ of 0.30 is displayed in Fig. 5 in comparison with the simulated mole fractions. The match between experimental and numerical results is as well acceptable and mostly within the range of accuracy of the experiments. The increase of the mole fractions with $Y_{Fuel,1}$ is well reproduced. The dependency of the mole fractions of these species on the strain rate a_2 is only little. Due to the near sooting limit conditions of the counter-flow diffusion flames the mole fractions of higher PAHs are below the detection limit of the applied sampling and GC/MS-method. Therefore, experimental data for higher PAHs to compare with simulations are not available. According to the recent work of Dong et al. [61], PAH predictions are known to have large uncertainties, which for benzene range up to a factor of 5 and for larger species even up to a factor of 10. However, this statement holds for the application of one comprehensive reaction mechanism (MAH/PAH subset of the C3MechV3.3) to a variety of complex aliphatic and aromatic fuels and mixtures of them [61]. From Figs. 4d and 5 predictions of A1, A2R5 and A2 generally better than ±50% compared with experimental values can be seen. The reasons for this are the near sooting limit conditions for the experiments producing PAHs in low concentrations, and the comparatively simple single fuel C_2H_4, the combustion of which including the reaction pathways to A1 and PAHs is well described by the reaction mechanism implemented in the ABF-model.

4.2. Soot formation and particle dynamics

Soot formation from the precursor molecules in these flames occurs between the flame zone and the stagnation plane. Fig. 6 compares the soot volume fractions obtained by SMPS and 2C-TiRe-LII with simulations employing the ABF-model for the flames with mass fraction of fuel $Y_{Fuel,1} = 0.25$ and $Y_{Fuel,1} = 0.35$, at $a_2 = 60\ s^{-1}$. Considering the experimental errors and spatial resolution, the experimental values from SMPS and 2C-TiRe-LII fairly agree. The extension of the soot volume fraction profile towards the fuel duct which is observed for the 2C-TiRe-LII measurements can be traced back to the slight bending of the flame due to exhaust gas removal.

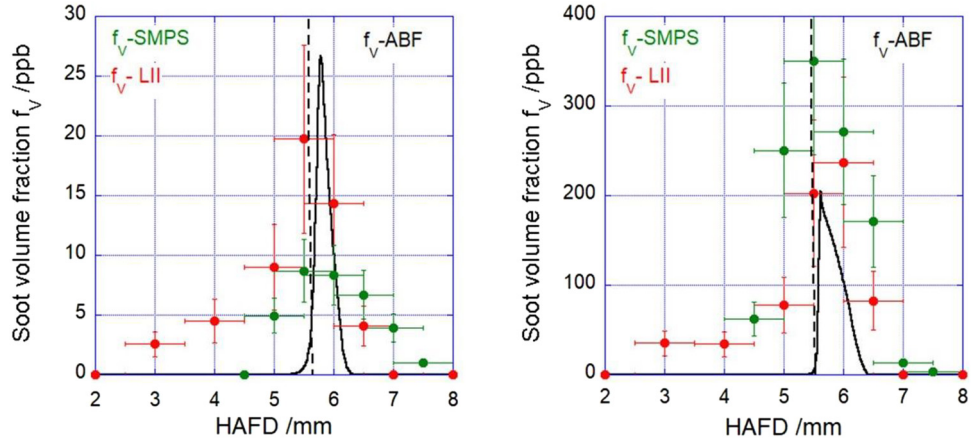

Fig. 6. Axial soot volume fraction profiles for the counter-flow diffusion flame with $Y_{Fuel,1} = 0.25$ (left), $Y_{Fuel,1} = 0.35$ (right) and $a_2 = 60\ s^{-1}$; symbols indicate experimental results, error bars represent estimations of uncertainties according to the spatial resolution and accuracy of the measurements; lines represent numerical simulations; the stagnation plane is indicated by the black dotted lines.

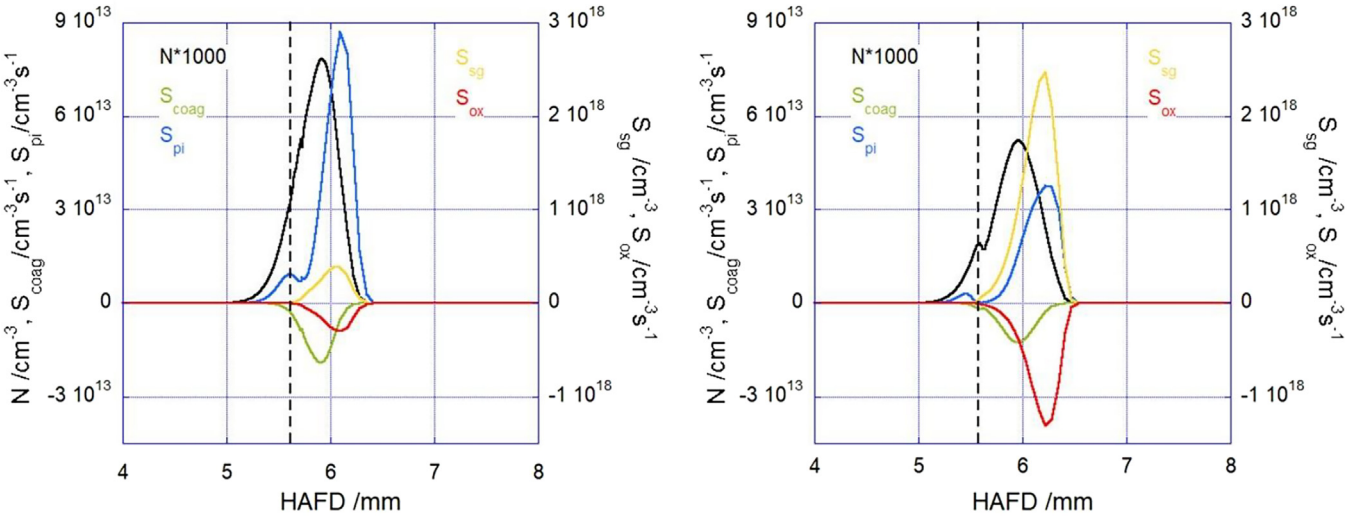

Fig. 7. Profiles of source terms of the moment balance equations for particle inception (S_{pi}), coagulation (S_{coag}), surface growth (S_{sg}), and oxidation (S_{ox}) for the counter-flow diffusion flame with $Y_{Fuel,1} = 0.25$ (left) and $Y_{Fuel,1} = 0.35$(right) at $a_2 = 60\ s^{-1}$; the stagnation plane is indicated by the black dotted line.

The ABF-model reproduces the experimental values reasonably well, the deviation from the experimental values lies within the differences from the two applied experimental techniques. The experimental profiles are broader than the computed profiles owing to the spatial resolution of the probe and the laser technique. The shape of the profiles and the position of the peak values agree well. The shapes of the calculated profiles also agree well with the ones reported in refs [6,14] simulated with the respective soot models, while the absolute values are in the same order of magnitude, however, differing due to different $Y_{Fuel,1}$ and strain rates a_2.

Soot formation is induced by particle inception at the position, where the aromatic hydrocarbons and C_2H_2 exhibit their peak mole fractions and soot formation is enhanced by mainly surface growth reactions in that region, see Fig. 7. Growing number densities of soot particles force particle coagulation leading to peak number densities slightly below the position of peak surface growth rates. Surface growth and particle inception continue with decreasing rates towards the stagnation plane causing the appearance of the peak soot volume fraction slightly above the stagnation plane. Interestingly, in the stagnation plane region and slightly below particle inception and surface growth prevail at low rates, indicated by a little pronounced peak in number density, inception and coagulation rates. Similar profiles of number density are simulated in ref. [6]. This is due to the comparatively high temperature in this region and the presence of soot precursor molecules and surface growth species, whereas no oxidation occurs. This behavior suggests different types of particles along the HAFD for the counter-flow diffusion flames. Above the stagnation plane where oxygen is present, soot particles formed at high rates through particle inception and surface growth are partially oxidized at high oxidation rates. Near the stagnation plane at decreasing oxygen mole fractions soot particles mature by further surface growth and coagulation, whereas even below the stagnation plane particle inception and PAH adsorption continues leading to particles not having experienced oxidative attack. These different types of soot particles should be made visible also through SMPS and 3WE-TiRe-LII.

This figure does not change qualitatively when varying the fuel mass fraction $Y_{Fuel,1}$, see Fig. 7. Increasing the mass fraction of fuel $Y_{Fuel,1}$ broadens the soot formation zone leading to more inception soot despite somehow lower peak inception rates. Due to increasing mole fractions of C_2H_2 and PAHs, surface growth rates and adsorption rates increase considerably. Correspondingly, higher soot volume fractions are observed, and coagulation produces particles with slightly larger CMD.

The measured peak soot volume fractions increase from about 10 ppb at $Y_{Fuel,1} = 0.20$ to about 200 ppb at $Y_{Fuel,1} = 0.35$. The variation of peak soot volume fractions with $Y_{Fuel,1}$ measured by SMPS is stronger than that detected with 2C-TiRe-LII, while the latter is well reproduced by the numerical simulations. The sensitivity $d\log(f_{V,max})/dY_{Fuel,1}$ amounts to about 8.7 at $Y_{Fuel,1} < 0.25$ and 8.9 at $Y_{Fuel,1} > 0.25$ at strain rates $a_2 = 60\ s^{-1}$. As far as similar values of $Y_{Fuel,1}$ have been operated, measured peak soot volume fractions in ref. [14] are comparable, with a somehow smaller sensitivity $d\log(f_{V,max})/dY_{Fuel,1}$ of 3.5 at $0.2 < Y_{Fuel,1} < 0.4$ at $a_2 = 60\ s^{-1}$.

An inverse effect is observed when increasing the strain rate a_2 of the counter-flow diffusion flames. Increasing the strain rate pushes the different flame zones together reducing reaction times along the central streamline and the particle inception zone, particle oxidation zone, and surface growth zone coincide to a larger extent. Thereby, particle inception rates increase leading to higher particle number densities of particles with smaller CMD and, therefore, lower soot volume fractions. This trend is documented in Fig. 8, right, where the peak soot volume fractions are plotted versus the strain rate for flames with the fuel mass fraction of $Y_{Fuel,1} = 0.3$. A clear decrease of the peak soot volume fractions with increasing strain rate is obvious from the figure. The decreasing peak soot volume fraction is accompanied by only a slight decrease in the peak mole fractions of the soot precursor molecules C_2H_2, A1, A2R5, A2, compare Fig. 5. The lower peak soot volume fractions with increasing strain rate a_2 are caused mainly by oxidation through the increased oxygen mole fraction in the soot forming region. The trend is reproduced well by the ABF-model and the deviations lie within the experimental uncertainties or are lower than the differences of the experimental values from 2C-TiRe-LII and SMPS, respectively. At $Y_{Fuel,1} = 0.30$ the sensitivity $d\log(f_{V,max})/da_2$ amounts to about 0.007 at $a_2 < 40\ s^{-1}$ and 0.029 for $a_2 > 40\ s^{-1}$, which compares well with the results reported in [14].

The axial profiles of the CMDs, see Fig. 9, upper left, reflect the soot particle dynamics occurring in the counter-flow diffusion flames: Soot formation is induced by particle inception at the positions, where the soot precursor molecules exhibit their peak mole fractions and is enhanced by mainly surface growth reactions in that region 1 mm to 1.5 mm above the stagnation plane.

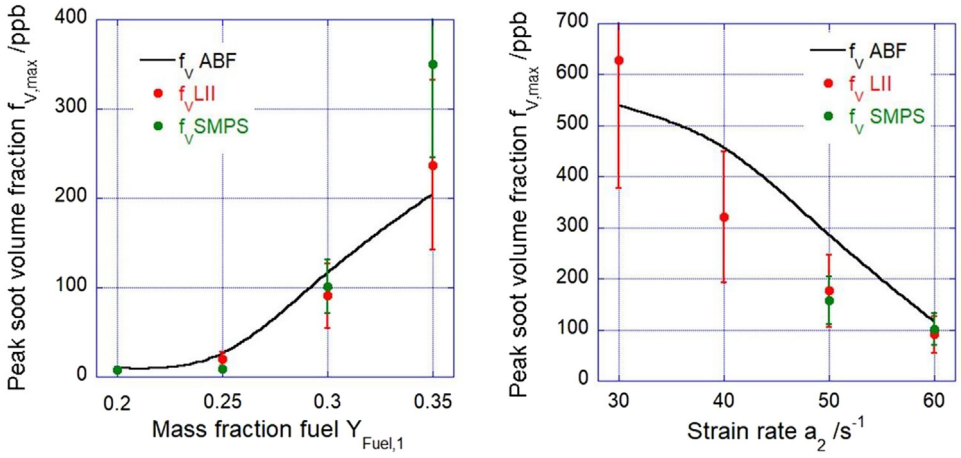

Fig. 8. Peak soot volume fractions in dependence on $Y_{Fuel,1}$ at a strain rate $a_2 = 60\ s^{-1}$ (left) and in dependence on a_2 at $Y_{Fuel,1} = 0.30$ (right); symbols indicate experimental results, error bars represent estimations of uncertainties according to the accuracy of the measurements; lines represent numerical simulations with the ABF-model.

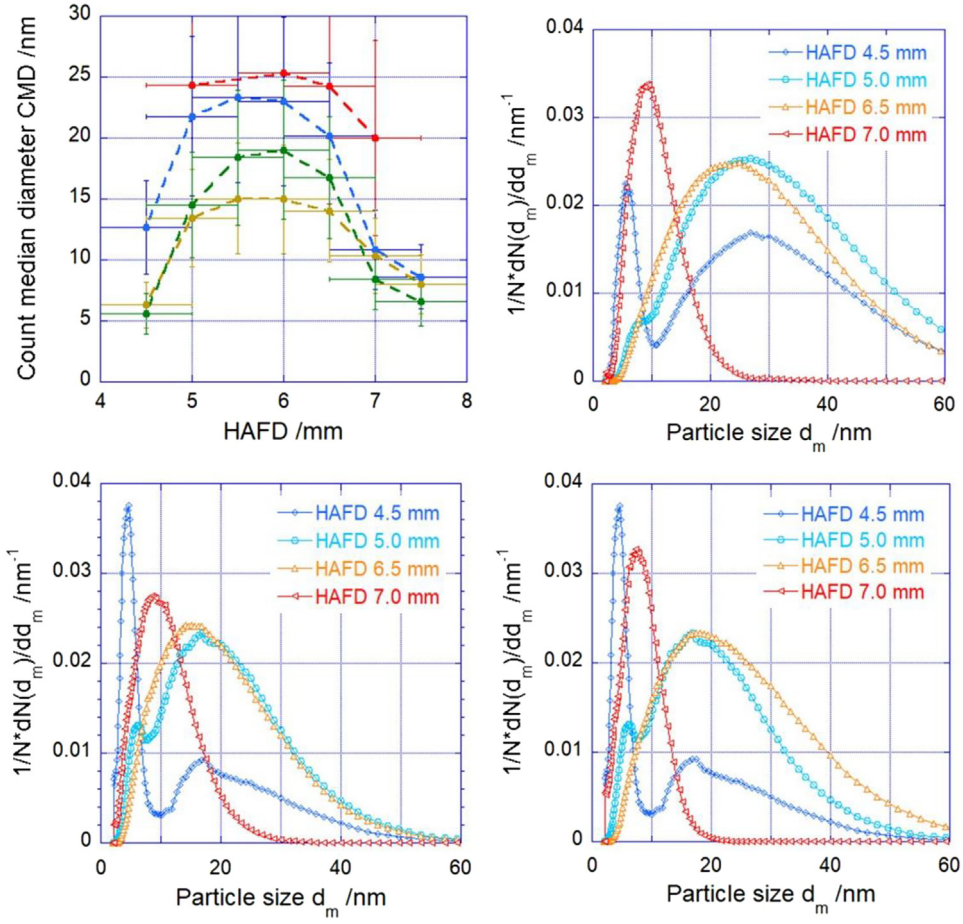

Fig. 9. Axial profiles of the CMDs for the flames with $Y_{Fuel,1} = 0.35$ at $a_2 = 60\ s^{-1}$ from 2C-TiRe-LII (red symbols), $Y_{Fuel,1} = 0.35$ at $a_2 = 60\ s^{-1}$ from SMPS (blue symbols), $Y_{Fuel,1} = 0.30$ at $a_2 = 60\ s^{-1}$ from SMPS (yellow symbols), $Y_{Fuel,1} = 0.30$ at $a_2 = 50\ s^{-1}$ from SMPS (green symbols), upper left; the error bars represent estimations according to the accuracy of the measurements. Particle size distributions from SMPS for the flame with $Y_{Fuel,1} = 0.35$ at $a_2 = 60\ s^{-1}$, upper right, and $Y_{Fuel,1} = 0.3$ at $a_2 = 60\ s^{-1}$, lower left, and $Y_{Fuel,1} = 0.3$ at $a_2 = 50\ s^{-1}$, lower right.

Particle growth occurs rapidly essentially through coagulation and soot particles are convected by the oxidizer flow towards the stagnation plane. Consequently, the CMDs increase and attain peak values in that region. Particle inception and surface growths continues in the region below the stagnation plane at slower rates, leading to small particles being convected with the fuel flow towards the stagnation plane and growing during their convective transport. Note that the time scale is not linear to HAFD, so that residence times for particle dynamics along the axial streamline increase to very large values when approaching the stagnation plane. The maximum CMDs increase with increasing peak soot volume fraction and decrease with increasing strain rate. The measured particle sizes obtained through SMPS agree well with the ones obtained by 2C-TiRe-LII within the limits of accuracy of the

experimental methods. Due to the coarse spatial resolution of the LII-experiments and particle probing, the widths of measured profiles may be oversized.

From the discussion of Fig. 7 different types of particles in the fuel flow below the stagnation plane and oxidizer flow above the stagnation plane have been suggested. These fundamental differences are obvious from the particle size distributions obtained through SMPS for particles generated in the oxidizer flow (HAFD > 6 mm) and those growing in the fuel flow (HAFD < 5 mm), see Fig. 9. While the former show monodispersed size distributions, which can be approximated well by log-normal distribution functions, the latter ones have bimodal size distributions with a sharp maximum below 5 nm to 10 nm and a second maximum near 20 nm. The shapes of the size distributions for particles in the oxidizer flow remain monomodal, but the width of the distribution decreases when moving further upstream in the oxidizer flow. This is the result of the oxidation of the particles at fast rates and shifting thereby the distribution function to smaller sizes and narrowing the size distributions. This is not observed for particles generated in the fuel flow. Here, small particles, possibly liquid-like nascent particles, exist along with relatively large particles of sizes in the order of magnitude of 20 nm. These small particles coagulate with larger ones resulting in reduced number densities and a shift of the size distribution to larger values when approaching the stagnation plane. The small liquid-like particles are not captured by 2C-TiRe-LII, because they scarcely absorb light in the NIR region (λ = 1064 nm). This may be also a reason for differences in the experimental results from SMPS and 2C-TiRe-LII [32]. The bimodal size distributions also explain the differences between the results from 2C-TiRe-LII and SMPS when calculating of the CMDs on the basis of lognormal distribution functions.

4.3. Optical particle properties

The absorption of light following Bouguer-Lambert-Beer's law and neglecting Rayleigh scattering for molecules, clusters and small particles, is given by

$$a(\lambda) = \ln\left(\frac{I(\lambda)}{I_0(\lambda)}\right) = -\,\sigma(\lambda)\cdot\ f_V\cdot\ L, \tag{10}$$

where $a(\lambda)$ means the absorbance, $\sigma(\lambda)$ the absorption cross section, L the optical path length of the experiment and f_V the soot volume fraction. Using the Rayleigh approximation, $d_P \ll \lambda$, where d_P is the particle diameter and λ the absorption wavelength for spherical particles, $\sigma(\lambda)$ can be expressed as

$$\sigma(\lambda) = \frac{\pi^2 d_P^3}{\lambda} E(m,\ \lambda). \tag{11}$$

According to Eq. (11) the absorbance at a wavelength λ is high if the refractive index function of absorption at this wavelength is high. For experiments with identical mass concentration and optical path length at two wavelengths, Eq. (11) results in

$$\frac{\sigma(\lambda_1)\cdot\lambda_1}{\sigma(\lambda_2)\cdot\lambda_2} = \frac{E(m,\lambda_1)}{E(m,\lambda_2)}. \tag{12}$$

If then $E(m,\lambda_{UV})/E(m,\lambda_{NIR})$ is large for $\lambda_1 = \lambda_{UV}$ and $\lambda_2 = \lambda_{NIR}$, particles absorb stronger in the UV as compared to NIR and vice versa. The same holds for $E(m,\lambda_{VIS})/E(m,\lambda_{NIR})$, and $E(m,\lambda_{UV})/E(m,\lambda_{VIS})$ and the respective wavelengths.

Figure. 10 displays the axial profiles of the ratios $E(m,\lambda_{UV})/E(m,\lambda_{NIR})$ and $E(m,\lambda_{VIS})/E(m,\lambda_{NIR})$ for the counter-flow flame with $Y_{Fuel,1}$ = 0.35 and a_2 = 60 s^{-1} along with the soot volume fractions obtained from SMPS. The ratio $E(m,\lambda_{UV})/E(m,\lambda_{NIR})$ is throughout higher than $E(m,\lambda_{VIS})/E(m,\lambda_{NIR})$ indicating a stronger absorption in the UV than in the VIS. In the region of peak soot volume fractions and larger primary particle sizes the ratios

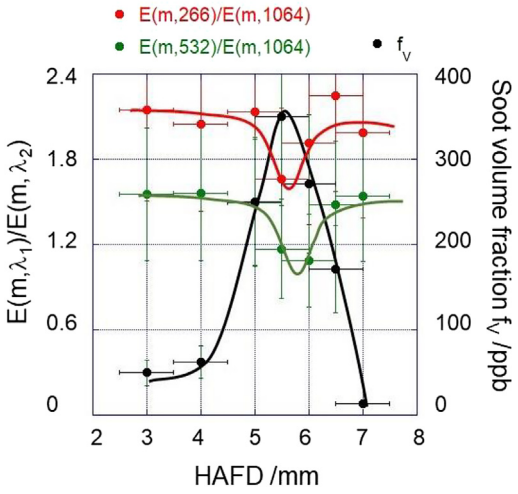

Fig. 10. Axial profiles of $E(m,\lambda_1)/E(m,\lambda_2)$ and soot volume fraction for the counter-flow diffusion flame with $Y_{Fuel,1}$ = 0.35 at a_2= 60 s^{-1}; the error bars represent estimations according to the accuracy of the measurements and special resolution.

decrease revealing an increasing absorption in the NIR. Below the stagnation plain in the fuel flow and above the stagnation plane in the oxidizer flow, where small particles prevail, larger ratios $E(m,\lambda_1)/E(m,\lambda_2)$ are detected. The high value of $E(m,\lambda_{UV})/E(m,\lambda_{NIR})$ in the region below the stagnation plane in the fuel flow corroborates the presence of liquid-like particles absorbing in the UV as indicated by the particle size distributions in Fig. 9.

Figure. 11 displays the ratios $E(m,\lambda_{UV})/E(m,\lambda_{VIS})$, $E(m,\lambda_{UV})/E(m,\lambda_{NIR})$, and $E(m,\lambda_{VIS})/E(m,\lambda_{NIR})$ for the counter-flow flames with a_2 = 60 s^{-1} in dependence on $Y_{Fuel,1}$ in the fuel flow (left part) and in dependence on the strain rate a_2 for flames with $Y_{Fuel,1}$ = 0.3 (right part). The values have been collected at the positions of maximum particle size (HAFD ≈ 5.5 mm). The ratio $E(m,\lambda_{UV})/E(m,\lambda_{VIS})$ ranges about 1.5 and is only little dependent on the fuel mass fraction $Y_{Fuel,1}$ and strain rate a_2. In contrary, $E(m,\lambda_{UV})/E(m,\lambda_{NIR})$, and $E(m,\lambda_{VIS})/E(m,\lambda_{NIR})$ decrease reasonably with increasing $Y_{Fuel,1}$ and decreasing a_2 ranging between values of approximately 3 and 0.5. Especially $E(m,\lambda_{VIS})/E(m,\lambda_{NIR})$ agrees well with the values published in the literature ranging from 0.8 to 2.0 for matured soot particles to young soot particles [17,52,70-72,74] and for flame generated soot and commercial carbon black [18]. $E(m,\lambda_{UV})/E(m,\lambda_{VIS})$ and $E(m,\lambda_{UV})/E(m,\lambda_{NIR})$ measured by Yon et al. and Bejaoui et al. [53,72] also agree well with the values evaluated in this study. If E(m,633 nm) = 0.228, which has been used for the calibration of the LII signals, is taken as an approximation for $E(m,\lambda_{VIS})$, $E(m,\lambda_{UV}) \approx 0.33$ and $E(m,\lambda_{NIR}) \approx 0.11$ to 0.22 can be derived from the measured ratios. These values also agree well with data reported in the literature [54–56].

The value of ≈ 1.5 for $E(m,\lambda_{UV})/E(m,\lambda_{VIS})$ implies, that the absorption of light by the soot particles is stronger by a factor of about 3 at λ = 266 nm compared to the absorption at λ = 532 nm, see Eq. (11), without large variation with $Y_{Fuel,1}$ and a_2. A value of ≈ 2.5 for $E(m,\lambda_{UV})/E(m,\lambda_{NIR})$ points out, that the absorption of light by the soot particles is stronger by a factor of about 10 at λ = 266 nm compared to the absorption at λ = 1064 nm (see Fig. 11 at $Y_{Fuel,1}$ = 0.25 (left part) and a_2 = 60 s^{-1} (right part)). However, in the latter case and similarly for the ratio $E(m,\lambda_{VIS})/E(m,\lambda_{NIR})$ the values are strongly dependent on $Y_{Fuel,1}$ and a_2, resulting in values of ~ 1.5 at $Y_{Fuel,1}$ = 0.35 or ~ 0.75 at a_2 = 30 s^{-1}. This variation indicates a reasonable increase of the absorption in the NIR region for soot particles generated at high fuel mass fractions and low strain rates, i.e. high soot volume

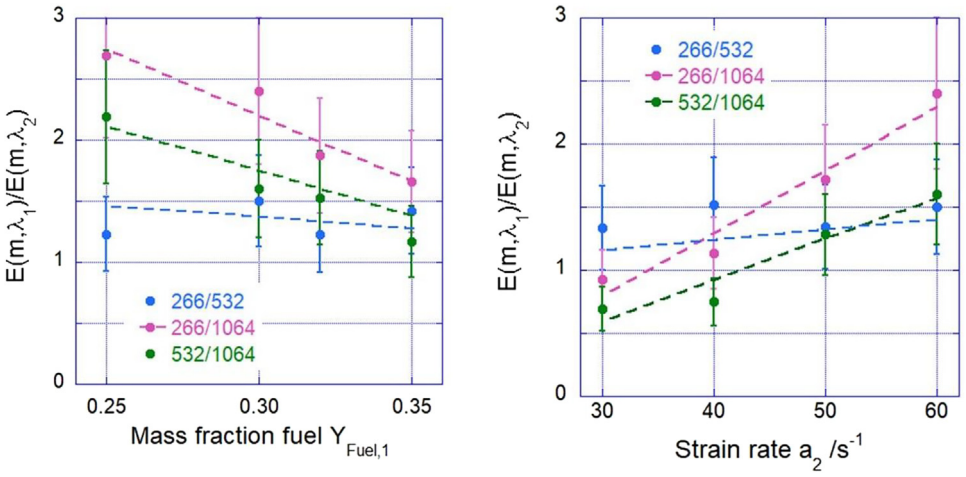

Fig. 11. $E(m,\lambda_{UV})/E(m,\lambda_{VIS})$, $E(m,\lambda_{UV})/E(m,\lambda_{NIR})$ and $E(m,\lambda_{VIS})/E(m,\lambda_{NIR})$ at 5.5. mm HAFD for the counter-flow diffusion flames with $a_2 = 60\ s^{-1}$ in dependence on $Y_{Fuel,1}$ (left part) and for the flame with $Y_{Fuel,1} = 0.3$ in dependence on the strain rate (right part); the error bars represent the standard deviations obtained from the 3WE-TiRe-LII experiments (see *Section 2.5.3*); dotted lines are linear approximations.

fractions f_V, see Fig. 8, connected with larger primary particle sizes. The $E(m,\lambda_{UV})/E(m,\lambda_{NIR})$ ratios reported here are quite similar to what can be calculated from the $E(m,\lambda)$ values derived from quantum confinement effects by Wan et al. [73], showing a decrease of the absorption coefficient and an increase of $E(m,\lambda_{UV})/E(m,\lambda_{NIR})$ ratio as the particle size becomes smaller.

The peak soot volume fractions appearing in the flames apparently determine the absorption behavior of the soot particles absorbing in the NIR region by affecting the molecular structures. Obviously, these structures are prevailing in large primary particles at high soot volume fractions as is documented by the variation with HAFD of the ratios $E(m,\lambda_{UV})/E(m,\lambda_{NIR})$ and $E(m,\lambda_{VIS})/E(m,\lambda_{NIR})$ for the counter-flow flame with $Y_{Fuel,1} = 0.35$ and $a_2 = 60\ s^{-1}$ in Fig. 10.

The ratios of refractive index functions for absorption have been determined by 3WE-TiRe-LII experiments at the wavelengths 266 nm, 532 nm and 1064 nm. Therefore, the signals arise from molecular structures absorbing light in the respective wavelength regions. Molecular structures not absorbing at these wavelengths are not contributing to the signals as discussed in [57]. As can be seen from the particle size distributions in Fig. 9 small particles in the size range of about 5 nm appear near the stagnation plane and below in the fuel flow. If these particles are liquid-like ensembles of large precursor molecules, they absorb scarcely at 532 nm and 1064 nm [18] and do not contribute to the LII signals and the measured ratios $E(m,\lambda_1)/E(m,\lambda_2)$ along HAFD. These small particles are not detected by this method.

4.4. Nanostructural properties

The refractive index function for absorption $E(m,\lambda)$ describes the absorption characteristics of soot particles and reflects their molecular and nanostructural properties. The basic structural units (BSUs) are stacked graphene-like layers within the primary particles [18,74-78]. The size L_f, curvature T_f, and separation distance $D_{s,f}$ of stacked graphene-like layers within primary particles affect the share of internal and edge carbon-sites as well as of sp2- and sp3-hybridized carbon atoms, and, therefore, the energy level of the graphene-like structures and their absorption behavior. Generally, a bathochromic shift of the absorption connected with a decrease of e.g., $E(m,\lambda_{UV})/E(m,\lambda_{NIR})$ with increasing size of the BSUs can be ascertained [17,19,74,75]. This behavior is reflected from the soot particles in the investigated counter-flow flames. Fig. 12 depicts examples of fringe size distributions for soot primary particles obtained from the evaluation of HRTEM images of soot particles collected from flames with different $Y_{Fuel,1}$ and a_2. The particles have been collected placing the TEM-grids at the position of peak soot volume fractions (≈ 5.5 mm HAFD). At this position the number density and the primary particle sizes are highest (compare Figs. 6 and 9), so that in spite of the size of the TEM-grids (≈ 3.0 mm diameter), particles with properties representative for this position are collected.

The figure also shows the HRTEM images of evaluated regions within the primary particles. The measured values of $E(m,\lambda_{UV})/E(m,\lambda_{NIR})$ at the positions of peak soot volume fractions are also given. The examples clearly demonstrate a broadening of the fringe size distributions to larger sizes with decreasing strain rate a_2 and increasing fuel mass fraction $Y_{Fuel,1}$. Also, a noticeable decrease of $E(m,\lambda_{UV})/E(m,\lambda_{NIR})$ with increasing fringe size is obvious from Fig. 12. Most striking, the appearance of large sized BSUs relates to increasing peak soot volume fractions of the flames. These dependencies are detailed in Fig. 13 for the mean fringe size $L_{f,m}$, decile of the fringe size $L_{f,90}$, and maximum fringe size $L_{f,max}$. For the evaluation of these statistical values of the fringe size distributions up to 10 distributions such as exemplarily displayed in Fig. 12 have been averaged.

The mean fringe sizes $L_{f,m}$ range between about 4.5 Å and 5.5 Å, whereas the decile $L_{f,90}$ of the fringe sizes, which represents 90% of the BSUs ranges between 6.5 Å and 8.5 Å. However, the primary particles also contain fringes up to about 17 Å to 28 Å (maximum values $L_{f,max}$) appearing at low frequencies. Fringes of similar size have been detected in flame generated soot [76] and soot collected from the exhaust of internal combustion engines [77,78]. The dependency of the fringe sizes on peak soot volume fraction appears approximately linear.

The approximate linear correlation between peak soot volume fraction and the fringe sizes on the one hand and the ratio of refractive index functions for absorption $E(m,\lambda_{UV})/E(m,\lambda_{NIR})$ on the other also results in an approximate linear dependency of the ratio of refractive index functions for absorption and the fringe sizes. This has been detected also in previous work, see e.g. [18,19]. The broad variation of refractive index function for absorption or its ratios at different wavelengths reported in the literature [17,52,70-74] may find its explanation in this dependency. The extension of the fringes also determines the reactivity of soot against oxidation by O_2 and an approximate linear correlation of a reactivity index with reciprocal fringe sizes has been reported in [18]. The characteristic statistical values of the fringe size distributions determine

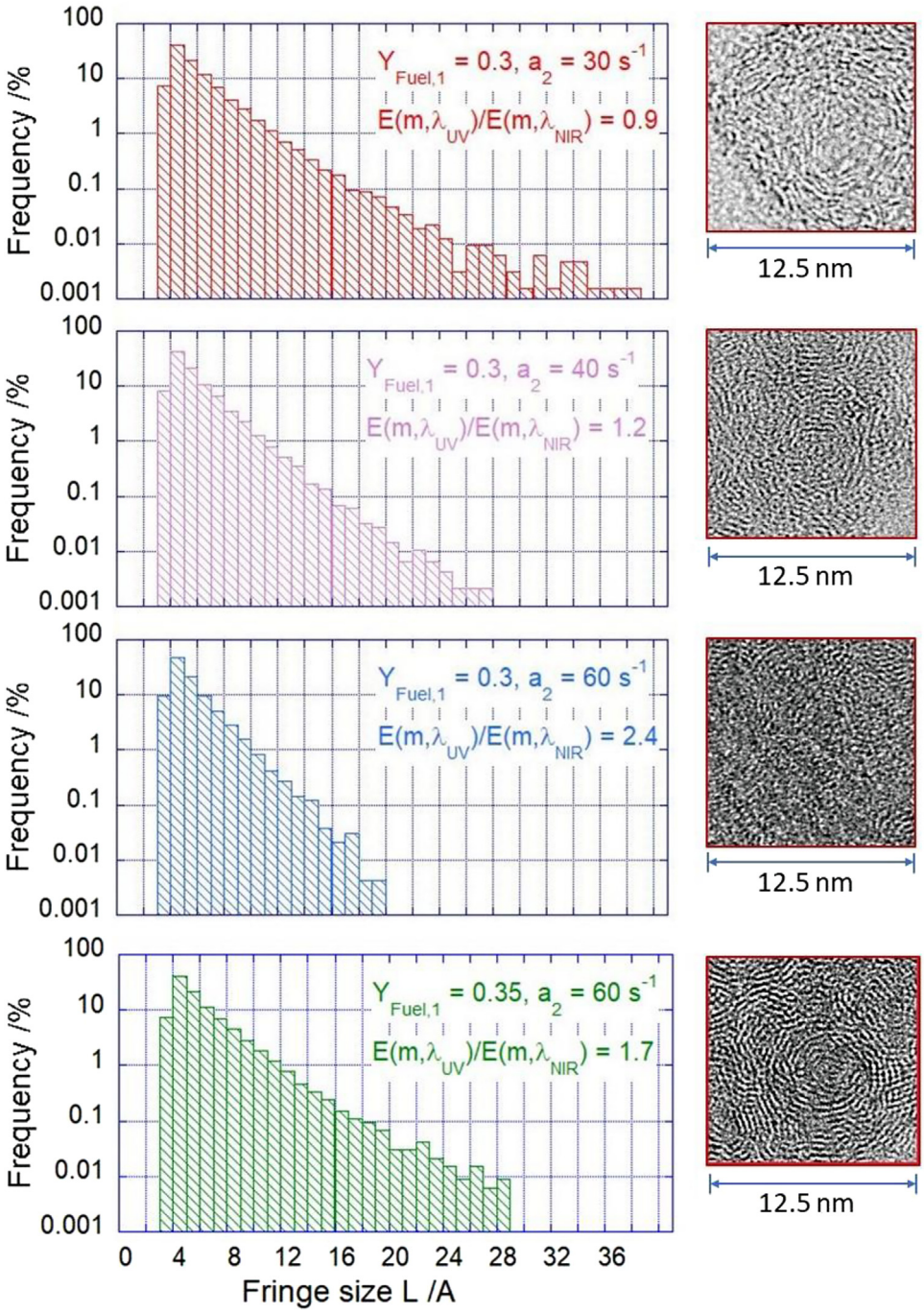

Fig. 12. Examples of fringe size distributions as obtained from HRTEM images for soot primary particles collected from flames with different fuel mass fractions and strain rates.

the properties of the nanosized particles and are easily accessible via $E(m,\lambda_2)/E(m,\lambda_2)$, offering a method of characterizing functional nanoparticles, e.g. their reactivity. On the other hand, the fringe extension sheds light on the environment of soot particles during their origin, e.g. concentration of PAHs.

According to the fringe size distributions and their characteristic statistical values, respectively, the largest part of the BSUs in the primary particles ($L_{f,90}$) exhibits sizes increasing with the peak soot volume fraction $f_{V,max}$ up to sizes in the order of magnitude of 7 Å to 10 Å, compare the size of coronene units ≈ 7 Å. Similar sizes of the BSUs determined with different methods are reported from literature, see e.g., the review in ref. [79] and references therein. This is consistent with the mole fractions of pre-particle species and the rates of particle inception presented in Figs. 5 and 7. The mole fractions of the soot precursors C_2H_2, A1, A2R5 increase by about 30% to 40%, when the peak soot volume fraction increases from about 100 ppb to 300 ppb, see Figs 5. This holds also for the larger precursors A2, A3 (phenanthrene), A4 (pyrene). The increase of the mole fractions of these components causes a similar increase of the surface growth rates, which is the strongest soot mass source with the main channel occurring via reactions with C_2H_2, and PAH adsorption. Surface growth reactions on stacked PAHs/soot precursors contribute reasonably to their mass growth. For example, the growth of pyrene (extension ≈ 6 Å x 4.8 Å) to coronene

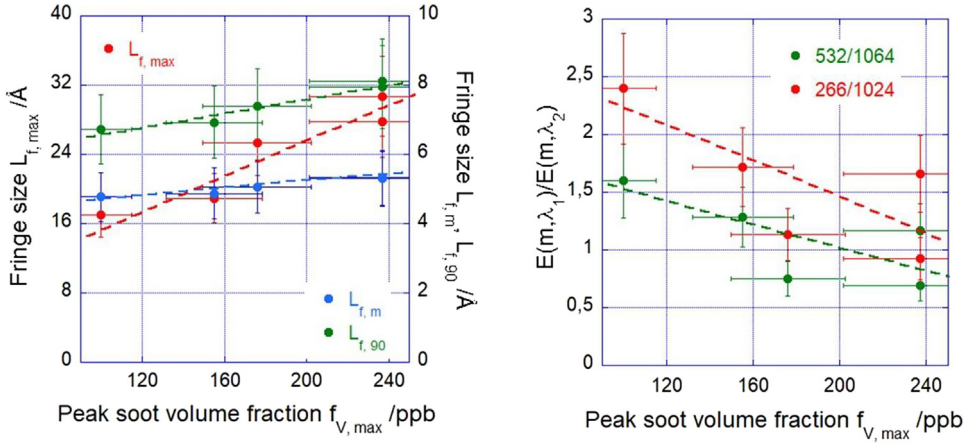

Fig. 13. Mean fringe size $L_{f,m}$, decile 9 of the fringe size $L_{f,90}$, and maximum fringe size $L_{f,max}$ (left) as well as $E(m,\lambda_{VIS})/E(m,\lambda_{NIR})$ and $E(m,\lambda_{UV})/E(m,\lambda_{NIR})$ (right) in dependence on the peak soot volume fractions $f_{V,max}$ as determined by SMPS for soot primary particles collected from flames with different $Y_{Fuel,1}$ and a_2; the error bars reflect the standard deviations from the evolution of the fringe size distributions and the experimental uncertainties in the determination of $f_{V,max}$ from SMPS; the dotted lines represent linear approximations.

(extension ≈ 7 Å) increases the mass by about 48% and the increase of mass varies with the square of the size. These findings are consistent with experimental results based on photo ionization time of flight mass spectroscopy [80], where species in the mass range from 200 amu to 400 amu are detected and periodically appearing multiples of these are assigned to stacked PAHs. Also, large aromatic structures connected via aliphatic connections and bridges as discussed in ref. [81] fit into this picture, because the interruption of aromatic structures by aliphatic strands limits the absorption of light in the visible and near infrared to the largest not disturbed aromatic structure.

5. Conclusions

In this work sooting counter-flow diffusion flames of C_2H_4/air have been investigated applying a multitude of experimental methods and numerical simulations. The focus is on flames with soot volume fractions near the sooting limit (f_V < 500 ppb) to shed light on the transition of precursor molecules on the molecular scale to primary soot particles and their nanostructure on the μm- and sub-μm scales. The operating parameters of the counter-flow flames have been set to establish a soot formation (SF) flame with the flame and soot formation region in the oxidizer flow above the stagnation plane.

The experimental techniques cover non-intrusive methods such as 2C-TiRe-LII and 3WE-TiRe-LII for the determination of soot volume fractions, primary particle sizes, and refractive index functions for absorption and their ratios at different wavelengths, respectively. Non-intrusive techniques have been complemented by intrusive ones, such as sampling with microprobes and analysis of gas composition by GC/MS, and particle sizing by SMPS and HRTEM. Also, the nanostructures of soot particles are obtained from analyzing HRTEM-images. For numerical simulations, the well-known ABF-model has been applied.

The main results can be summarized as follows: The structure of the counter-flow diffusion flames as determined by the measured temperatures, mole fractions of the major species, minor species, soot precursor molecules (as far as detectable) could be well reproduced within the experimental uncertainties by the ABF-model for varying fuel mass fractions and strain rates. Soot volume fractions at the applied low sooting conditions are also reproduced reasonably within the differences between the applied experimental methods via the ABF-model. The numerical simulations identify the different processes during particle formation. The main variation is attributed to variation of surface growth rates when applying strain rates and fuel mass fractions leading to higher soot volume fractions.

Particle sizing by 2C-TiRe-LII and SMPS gives results agreeing within the experimental uncertainties. Particle size distributions in the fuel rich region near and below the stagnation plane appear bimodal with a distinct maximum at particles sizes about 5 nm and 20 nm. The small particles presumably not absorbing light in the NIR region (λ = 1064 nm) due to a liquid like state are not captured by 2C-TiRe-LII.

The nanostructure of the primary particles exhibits BSUs with increasing fringe sizes up to the size of 7 Å to 10 Å when soot volume fractions increase from about 100 ppb to 300 ppb. This coincides with the increase of the mole fractions and the size of the detectable soot precursors with increasing soot volume fraction.

The ratios of $E(m,\lambda_{UV})/E(m,\lambda_{VIS})$, $E(m,\lambda_{VIS})/E(m,\lambda_{NIR})$, and $E(m,\lambda_{UV})/E(m,\lambda_{NIR})$ as determined by 3WE-TiRe-LII agree well with values reported in the literature. The value of $E(m,\lambda_{UV})/E(m,\lambda_{VIS})$ varies only slightly with the peak soot volume fraction in the flames, pointing out small sized nanostructures absorbing in the short wavelength range being contained to a large part in soot primary particles at all soot volume fractions. In contrary, the ratios $E(m,\lambda_{VIS})/E(m,\lambda_{NIR})$, and $E(m,\lambda_{UV})/E(m,\lambda_{NIR})$ decrease approximately linear with increasing soot volume fractions, pointing out nanostructures with increasing sizes absorbing in the visible and near infrared wavelength region. This finding applies not only to the variation of flame conditions studied, but also along the flame axis: In the region of peak soot volume fractions and larger primary particle sizes the ratios decrease revealing an increasing absorption in the NIR.

This is corroborated by the analysis of HRTEM-images that clearly bring about increasing sized BSUs with increasing soot volume fractions causing a shift of the absorption to larger wavelengths. The dependence of $E(m,\lambda_{VIS})/E(m,\lambda_{NIR})$ and $E(m,\lambda_{UV})/E(m,\lambda_{NIR})$ on the soot volume fraction may be the reason for the wide ranges of refractive index function for absorption and their ratios referenced in the literature.

Declaration of Competing Interest

The authors declare that they have no known competing financial interests or personal relationships that could have appeared to influence the work reported in this paper.

Acknowledgements

The authors are very grateful to the German Research Foundation (DFG) for financial support within the research projects TR470/7-1/2, SU249/6-1/2 and for experimental equipment within the HBFG program INST 121384/178–1 FUGG. In addition, this work has received funding from the Clean Sky 2 JU under European Union's Horizon 2020 research and innovation program (G.A. No. 821418, ESTiMatE).

The authors would like to thank Dr. Heike Störmer from the Laboratory for Electron Microscopy (Karlsruhe Institute of Technology (KIT)) for preparing electron microscopy images. Maurus Bauer is acknowledged for his excellent assistance in setting up the 3WL-TiRe-LII and performing the experiments.

References

[1] H. Bockhorn, T. Schäfer, Growth of soot particles in premixed flames by surface reactions, Soot Formation in Combustion – Mechanisms and Models, Springer-Verlag, Berlin Heidelberg (1994), p. 253.
[2] R.J. Kee, J.A. Miller, G.H. Evans, G. Dixon-Lewis, A computational model of the structure and extinction of strained, opposed flow premixed methane-air flames, Proc. Comb. Inst. 22 (1988) 1479–1495.
[3] Y. Wang, S.H. Chung, Soot formation in laminar counterflow flames, Prog. Energy Combust. Sci. 74 (2019) 152–238.
[4] K. Gleason, F. Carbone, A. Gomez, Effect of temperature on soot inception in highly controlled counterflow ethylene diffusion flames, Combust. Flame 192 (2018) 283–294.
[5] K. Gleason, F. Carbone, A. Gomez, PAHs controlling soot nucleation in 0.101-0.811 MPa ethylene counterflow diffusion flames, Combust. Flame 227 (2021) 384–395.
[6] L. Xu, F. Yan, M. Zhou, Y. Wang, S.H. Chung, Experimental and soot modeling studies of ethylene counterflow diffusion flames: non-monotonic influence of the oxidizer composition on soot formation, Combust Flame 197 (2018) 304–318.
[7] Y. Wang, S.H. Chung, Effect of strain rate on sooting limits in counterflow diffusion flames of gaseous hydrocarbon fuels: sooting temperature index and sooting sensitivity index, Combust. Flame 161 (2014) 1224–1234.
[8] U. Vandsburger, I. Kennedy, I. Glassman, Sooting counter-flow diffusion flames with varying velocity gradients, Proc. Comb. Inst. 20 (1985) 1105–1112.
[9] D.Du H.Wang, C. Sung, C.K. Law, Experiments and numerical simulation on soot formation in opposed-jet ethylene diffusion flames, Proc. Comb. Inst. 26 (1996) 2359–2368.
[10] M.E. Decroix, W.L. Roberts, Transient flow field effects on soot volume fraction in diffusion flames, Combust. Sci. Technol. 160 (2000) 165–189.
[11] H. Böhm, K. Kohse-Höeinghaus, F. Lacas, C. Rolon, N. Darabiha, S. Candel, On PAH formation in strained counterflow diffusion flames, Combust. Flame 124 (2001) 127–136.
[12] M. Yamamoto, S. Duan, S. Senkan, The effect of strain rate on polycyclic aromatic hydrocarbon (pah) formation in acetylene diffusion flames, Combust. Flame 151 (2007) 532–541.
[13] Y. Wang, S.H. Chung, Strain rate effect on sooting characteristics in laminar counterflow diffusion flames, Combust. Flame 165 (2016) 433–444.
[14] S. Kruse, A. Wick, P. Medwell, A. Attili, J. Beeckmann, H. Pitsch, Experimental and numerical study of soot formation in counterflow diffusion flames of gasoline surrogate components, Combust. Flame 210 (2019) 159–171.
[15] E. Quadarella, J. Guo, H.G. Im, A consistent soot nucleation model for improved prediction of strain rate sensitivity in ethylene/air counterflow flames, Aerosol Sci. Techn. 56 (2022) 636–654.
[16] https://www.adelaide.edu.au/cet/isfworkshop/.
[17] E. Therssen, Y. Bouvier, C. Schoemaecker-Moreau, X. Mercier, P. Desgroux, M. Ziskind, C. Focsa, Determination of the ratio of soot refractive index function E(m) at the two wavelengths 532 and 1064nm by laser induced incandescence, Appl. Phys. B 89 (2007) 417–427.
[18] F.P. Hagen, D. Kretzler, T. Häber, H. Bockhorn, R. Suntz, D. Trimis, Carbon nanostructure and reactivity of soot particles from non-intrusive methods based on UV-VIS spectroscopy and time-resolved laser-induced incandescence, Carbon N Y 182 (2021) 634–654.
[19] F.P. Hagen, R. Suntz, H. Bockhorn, D. Trimis, Dual-pulse laser-induced incandescence to quantify carbon nanostructure and related soot particle properties in transient flows – Concept and exploratory study, Combust. Flame (2022) in press.
[20] J. Appel, H. Bockhorn, M. Frenklach, Kinetic modelling of soot formation with detailed chemistry and physics: laminar premixed flames of C2-hydrocarbons, Combust. Flame 121 (2000) 122–136.
[21] A.M. Valencia-Lopez, F. Bustamante, A. Loukou, B. Stelzner, D. Trimis, M. Frenklach, N.A. Slavinskaya, Effect of benzene doping on soot precursors formation in non-premixed flames of producer gas (PG), Combust. Flame 207 (2019) 265–280.
[22] S. Ahuja, D.L. Miller, Design of a constant tension thermocouple rake suitable for flame studies, Sci. Instrum. 64 (1998) 1358–1359.
[23] V. Cundy, J. Morse, D. Senser, Constant-tension thermocouple rake suitable for use in flame mode combustion studies, Sci. Instrum. 57 (1986) 1209–1210.
[24] C.R. Shaddix, Correcting thermocouple measurements for radiation loss: a critical review, Proc. 33rd Natl. Heat Transf. Conf (1999).
[25] M. Sentko, S. Schulz, B. Stelzner, C. Anderlohr, M. Vicari, D. Trimis, Experimental investigation of the pressure influence on flame structure of fuel-rich oxy–fuel methane flames for synthesis gas production, Fuel 286 (2021) 119377.
[26] Y. Karakaya, J. Sellmann, I. Wlokas, T. Kasper, Influence of the sampling probe on flame temperature, species, residence times and on the interpretation of ion signals of methane/oxygen flames in molecular beam mass spectrometry measurements, Combust. Flame 229 (2021) 111388.
[27] N. Hansen, T.A. Cool, P.R. Westmoreland, K. Kohse-Höinghaus, Recent contributions of flame-sampling molecular-beam mass spectrometry to a fundamental understanding of combustion chemistry, Prog. Energy Combust. Sci. 35 (2009) 168–191.
[28] B. Zhao, Z. Yang, J. Wang, M.V. Johnston, H. Wang, Analysis of Soot Nanoparticles in a Laminar Premixed Ethylene Flame by Scanning Mobility Particle Sizer, Aerosol Sci. Technol. 37 (2003) 611–620.
[29] A.D. Abid, J. Camacho, D.A. Sheen, H. Wang, Quantitative measurement of soot particle size distribution in premixed flames - The burner-stabilized stagnation flame approach, Combust. Flame 156 (2009) 1862–1870.
[30] J. Camacho, C. Liu, C. Gu, H. Lin, Z. Huang, Q. Tang, X. You, C. Saggese, Y. Li, H. Jung, L. Deng, I. Wlokas, H. Wang, Mobility size and mass of nascent soot particles in a benchmark premixed ethylene flame, Combust. Flame 162 (2015) 3810–3822.
[31] H. Shariatmadar, P.G. Aleiferis, R.P. Lindstedt, Particle size distributions in turbulent premixed ethylene flames crossing the soot limit, Combust. Flame (2022), doi:10.1016/j.combustflame.2021.111978.
[32] F.P. Hagen, P. Vlavakis, M. Seitz, T. Klövekorn, H. Bockhorn, R. Suntz, D. Trimis, Soot nanoparticle sizing in counterflow flames using in-situ particle sampling and differential mobility analysis verified with two-color time-resolved laser-induced incandescence, Proc. Combust. Inst. 39 (2022), doi:10.1016/j.proci.202.
[33] W.C. Hinds, Aerosol Technology. Properties, Behavior, and Measurement of Airborne Particles, John Wiley & Sons, Inc., USA, 1999.
[34] S.C. Wang, R.C. Flagen, Scanning Electrical Mobility Spectrometer, Aerosol Sci. Technol. 13 (1990) 230–240.
[35] G.A. Kelesidis, S.E. Pratsinis, Determination of the volume fraction of soot accounting for its composition and morphology, Proc. Combust. Inst. 38 (2021) 1189–1196.
[36] Ü.Ö. Köylü, C.S. McEnally, D.E. Rosner, L.D. Pfefferle, Simultaneous measurements of soot volume fraction and particle size /microstructure in flames using a thermophoretic sampling technique, Combust. Flame 110 (1997) 494–507.
[37] M.L. Botero, J. Akroyd, D. Chen, M. Kraft, J.R. Agudelo, On the thermophoretic sampling and TEM-based characterisation of soot particles in flames, Carbon N Y 171 (2021) 711–722.
[38] M. Kholghy, M. Saffaripour, X. Yip, M.J. Thomson, The evolution of soot morphology in a laminar coflow diffusion flame of a surrogate for Jet A-1, Combust. Flame 160 (2013) 2119–2130.
[39] F.P. Hagen, F. Hardock, S. Koch, N. Sebbar, H. Bockhorn, A. Loukou, et al., Why soot is not alike soot: a molecular/nanostructural approach to low temperature soot oxidation, Flow, Turbul. Combust. 106 (2021) 295–329.
[40] H. Bockhorn, H. Geitlinger, B. Jungfleisch, T. Lehre, A. Schön, T. Streibel, R. Suntz, Progress in characterization of soot formation by optical methods, Phys. Chem. Chem. Phys. 4 (2002) 3780–3793.
[41] C. Schulz, B.F. Kock, M. Hofmann, H. Michelsen, S. Will, B. Bougie, R. Suntz, G. Smallwood, Laser-induced incandescence: recent trends and current questions, Appl. Phys. B 83 (2006) 333–354.
[42] F. Liu, B.J. Stagg, D.R. Snelling, G.J. Smallwood, Effects of primary soot particle size distribution on the temperature of soot particles heated by a nanosecond pulsed laser in an atmospheric laminar diffusion flame, Int. J. Heat Mass. Trans. 49 (2006) 777–788.
[43] B.F. Kock, B. Tribalet, C. Schulz, P. Roth, Two-color time-resolved LII applied to soot particle sizing in the cylinder of a Diesel engine, Combust. Flame 147 (2006) 79–92.
[44] T. Lehre, B. Jungfleisch, R. Suntz, H. Bockhorn, Size distributions of nanoscaled particles and gas temperatures from time-resolved laser-induced-incandescence measurements, Appl. Opt. 42 (2003) 2021–2030.
[45] H.A. Michelsen, F. Liu, B.F. Kock, H. Bladh, A. Boiarciuc, M. Charwath, T. Dreier, R. Hadef, M. Hofmann, J. Reimann, S. Will, P.-E. Bengtsson, H. Bockhorn, F. Foucher, K.-P. Geigle, C. Mounaim-Rousselle, C. Schulz, R. Stirn, B. Tribalet, R. Suntz, Modeling laser-induced incandescence of soot: a summary and comparison of LII models, Appl. Phys. B 87 (2007) 503–521.
[46] M. Charwath, R. Suntz, H. Bockhorn, Constraints of two-colour TiRe-LII at elevated pressures, Appl. Phys. B 104 (2011) 427–438.
[47] L.A. Melton, Soot diagnostics based on laser heating, Appl. Opt. 23 (1984) 2201–2208.
[48] H.A. Michelsen, Understanding and predicting the temporal response of laser induced incandescence from carbonaceous particles, J. Chem. Phys. 118 (2003) 7012–7045.
[49] H. Bladh, J. Johnsson, N.-E. Olofsson, A. Bohlin, P.-E. Bengtsson, Optical soot characterization using two-color laser-induced incandescence (2C-LII) in the soot growth region of a premixed flat flame, Proc. Combust. Inst. 33 (2011) 641–648.
[50] H.A. Michelsen, C. Schulz, G.J. Smallwood, S. Will, Laser-induced incandescence: particulate diagnostics for combustion, atmospheric, and industrial applications, Prog. Energy Combust. Sci. 51 (2015) 2–48.

[51] F.J. Bauer, K.J. Daun, F.J. Huber, S. Will, Can soot primary particle size distributions be determined using laser-induced incandescence? Appl. Phys. B 125 (2019) 109.
[52] H.A. Michelsen, P.E. Schrader, F. Goulay, Wavelength and temperature dependences of the absorption and scattering cross sections of soot, Carbon 48 (2010) 2175–2191.
[53] J. Yon, R. Lemaire, E. Therssen, P. Desgroux, A. Coppalle, K.F. Ren, Examination of wavelength dependent soot optical properties of diesel and diesel/rapeseed methyl ester mixture by extinction spectra analysis and LII measurements, Appl. Phys. B 104 (2011) 253–271.
[54] S.C. Lee, C.L. Tien, Optical constants of soot in hydrocarbon flames, Proc. Combust. Inst. 18 (1981) 1159–1166.
[55] C.R. Shaddix, T.C. Williams, Soot structure and dimensionless extinction coefficient in diffusion flames: implications for index of refraction, Combustion–Generated Fine Carbonaceous Particles, Karlsruhe University Press, Karlsruhe (2007), pp. 17–33.
[56] H. Chang, T.T. Charalampopoulos, Determination of the wavelength dependence of refractive indices of flame soot, Proc R Soc London A 430 (1990) 577–591.
[57] M.R. Kholghy, Y. Afarin, A.D. Sediako, J. Barba, M. Lapuerta, C. Chu, J. Weingarten, B. Borshanpour, V. Chernov, M.J. Thomson, Comparison of multiple diagnostic techniques to study soot formation and morphology in a diffusion flame, Combust. Flame 176 (2017) 567–583.
[58] W. Pejpichestakul, E. Ranzi, M. Peluchi, A. Frassoldati, A. Cuoci, A. Parente, T. Faravelli, Examination of a soot model in premixed laminar flames at fuel rich conditions, Proc. Combust. Inst. 37 (2019) 1013–1021.
[59] M.E. Mueller, G. Blanquart, H. Pitsch, Hybrid methods of moments for modeling soot formation and growth, Combust. Flame 156 (2009) 1143-115.
[60] H. Wang, M. Frenklach, A detailed kinetic modeling study of aromatics formation in laminar premixed acetylene and ethylene flames, Combust. Flame 110 (1997) 173–221.
[61] S. Dong, S.W. Wagnon, L.P. Maffei, G. Kukkadapu, A. Nobili, Q. Mao, et al., A new detailed kinetic model for surrogate fuels: c3MechV3.3, Appl. Energy Combust. Sci. 9 (2022) 100043.
[62] G. Kukkadapu, D. Kang, S.C. Wagnon, K. Zhang, M. Mehl, M. Monge-Palacios, et al., Kinetic modeling study of surrogate components for gasoline, jet and diesel fuels: C7-C11 methylated aromatics, Proc. Combust. Inst. 37 (2019) 521–529.
[63] N.A. Slavinskaya, U. Riedel, S.B. Dworkin, M.J. Thomson, Detailed numerical modeling of PAH formation and growth in non-premixed ethylene and ethane flames, Combust. Flame. 159 (2012) 979–995.
[64] G. Kukkadapu, S.W. Wagnon, W.J. Pitz, N. Hansen, Identification of the molecular-weight growth reaction network in counterflow flames of the C3H4 isomers allene and propyne, Proc. Combust. Inst. 38 (2021) 1477–1485.
[65] M.V.Z. Smoluchowski, Mathematical theory of the kinetics of the coagulation of colloidal solutions, Z. Phys. Chem. 92 (1917) 129–135.
[66] M. Frenklach, S.J. Harris, Aerosol dynamics modelling using the method of moments, J. Colloid Interface Sci. 118 (1987) 252–261.
[67] A. Kazakov, M. Frenklach, Dynamic modeling of soot particle coagulation and aggregation: implementation with the method of moments and application to high-pressure laminar premixed flames, Combust. Flame 114 (1998) 484–501.
[68] A. Wick, M. Frenklach, H. Pitsch, Systematic assessment of the method of moments with interpolative closure and guidelines for its application to soot particle dynamics in laminar and turbulent flames, Combust. Flame 214 (2020) 450–463.
[69] R.J. Kee, F.M. Rupley, J.A. Miller, Chemkin-II: A Fortran Chemical Kinetics Package for the Analysis of Gas-Phase Chemical Kinetics, Sandia National Lab. Livermore, 1989, doi:10.2172/5681118.
[70] G. Cléon, T. Amodeo, A. Faccinetto, P. Desgroux, Laser induced incandescence determination of the ratio of the soot absorption functions at 532nm and 1064nm in the nucleation zone of a low pressure premixed sooting flame, Appl. Phys. B 104 (2011) 297–305.
[71] X. López-Yglesias, P.E. Schrader, H.A. Michelsen, Soot maturity and absorption cross sections, J Aerosol Sci 75 (2014) 43–64.
[72] S. Bejaoui, R. Lemaire, P. Desgroux, E. Therssen, Experimental study of the E(mk)</number>/E(m, 1064) ratio as a function of wavelength, fuel type, height above the burner and temperature, Appl. Phys. B 116 (2014) 313–323.
[73] K. Wan, X. Shi, H. Wang, Quantum confinement and size resolved modelling of electronic and optical properties of small soot particles, Proc. Combust. Inst. 38 (2021) 1517–1524.
[74] A.V. Eremin, E.V. Gurentsov, R.N. Kolotushkin, The change of soot refractive index function along the height of premixed ethylene/air flame and its correlation with soot structure, Appl. Phys. B 126 (2020) 125.
[75] B. Apicella, P. Pré, M. Alfè, A. Ciajolo, V. Gargiulo, C. Russo, A. Tregrossi, D. Deldique, J.-N. Rouzaud, Soot Nanostructure Evolution in Premixed Flames by High Resolution Electron Transmission Microscopy (HRTEM), Proc. Combust. Inst. 35 (2015) 1895–1902.
[76] R.L. Vander Wal, A.J. Tomasek, M.I. Pamphlet, C.D. Taylor, W.K. Thompson, Analysis of HRTEM images for carbon nanostructure quantification, J. Nanopart. Res. 6 (2004) 555–568.
[77] S.A. Pfau, A. La Rocca, E. Haffner-Staton, G.A. Rance, M.W. Fay, R.J. Brough, S. Malizia, Comparative nanostructure analysis of gasoline turbocharged direct injection and diesel soot-in-oil with carbon black, Carbon 139 (2018) 342–352.
[78] A. Zygogianni, M. Syrigou, A.G. Konstandopoulos, M. Kosoglou, Oxidative reactivity of particulate samples from different diesel combustion systems and its relation to structural and spectral characteristics of soot, Emiss. Control Sci. Technol. 5 (2019) 99–123.
[79] J.W. Martin, M. Salamanca, M. Kraft, Soot inception: carbonaceous nanoparticle formation in flames, Prog. Energy Combust. Sci. 88 (2022) 100956.
[80] J. Happold, H.-H. Grotheer, M. Aigner, Soot precursors consisting of stacked pericondensed PAHs, Combustion-Generated Fine Carbonaceous Particles, Karlsruhe University Press, Karlsruhe (2007), pp. 277–288.
[81] A. D'Anna, Particle inception and growth: experimental evidences and a modelling attempt, Combustion-Generated Fine Carbonaceous Particles, Karlsruhe University Press, Karlsruhe (2007), pp. 289–320.